PHYSICAL REVIEW D **106,** 114042 (2022)

Parton distribution functions and QCD coupling constant from LHC and non-LHC data

Majid Azizi,[1,*] Ali Khorramian,[1,†] and Saeid Paktinat Mehdiabadi[2,‡]
[1]*Faculty of Physics, Semnan University, P.O. Box. 35131-19111, Semnan, Iran*
[2]*Department of Physics, Yazd University, P.O. Box 89195-741, Yazd, Iran*

(Received 13 June 2022; accepted 13 December 2022; published 30 December 2022)

We present a new QCD analysis of parton distribution functions (PDFs) at next-to-leading order (NLO) and next-to-next-to-leading order (NNLO). In the present paper, the role of special types of experimental measurements for extracting PDFs is investigated, and simultaneously the values of the strong coupling constant are determined. Essential elements of this QCD analysis are the HERA combined data as a base, heavy-quark cross-section measurement together with Tevatron data on jet production and H1 and ZEUS jet cross sections as "non-LHC" data, and especially the "LHC" dataset for top-quark and jet cross sections. These different datasets have allowed detailed information at low x, providing worthwhile information on the nucleon's flavor, and have played an important role for some PDFs at large-x and strong coupling constant. Since the large-x gluon PDF benefits from an accurate determination of quark PDFs, we have enough motivation to focus on the top-quark production and jet cross-section measurements from LHC to find the impact of these data on the gluon PDF and strong coupling constant. These experimental data have an impact on the relative uncertainties of PDF. The gluon PDF at large x and the values of $\alpha_s(M_Z^2)$ are affected significantly. Although the main motivation of this paper is to focus on the gluon PDF and its uncertainty at large-x, giving notice to heavy PDF behavior in this region is also very important. We study the intrinsic charm (IC) using the BHPS model together with our extracted extrinsic charm PDF at large x, which can be very worthwhile for future experiments at the LHC.

DOI: 10.1103/PhysRevD.106.114042

I. INTRODUCTION

Great advances have been made in our knowledge of the parton substructure of the hadrons, with the accessibility of new high-energy scattering experimental data from different worldwide accelerators. Quantum chromodynamics (QCD) based on the quark-parton model has provided a reliable computational framework to describe the hadron interactions.

Basically, in standard factorization, parton distribution functions (PDFs) are specified using a comparison of theoretical QCD predictions with hard scattering experimental measurements covering a kinematic wide range in the Bjorken variable x and the momentum scale Q^2. However, these PDFs have generally been applied for the description of hadron structures. Within the context of the QCD quark-parton model, unpolarized and polarized PDFs have been considerably successful to describe a wide range of different processes. Very recently, the results of polarized QCD analysis of PDFs has been reported in Refs. [1–4]. It should be noted that modern PDFs are expected to deliver not only accurate information about the partons in a wide kinematic region of x and Q^2, but also information about the strong coupling constant α_s as a nonperturbative parameter. The value for this quantity is often correlated with the PDFs, and therefore they have to be extracted simultaneously in a QCD fit [5].

In recent years, various PDF sets [6–10] have been developed to be used at the Large Hadron Collider (LHC). These accurate PDFs have been applied for new physics searches [11–17], and also for the evaluation of PDF uncertainties on QCD precision observables. The PDF extracted results using different experimental measurements for both unpolarized and polarized QCD analysis are also reported in Refs. [18–33]. Very recently, the nuclear parton distribution functions (nPDFs) from a global QCD analysis at next-to-leading order (NLO) were also presented in Ref. [34].

---

[*] m.azizi@semnan.ac.ir
[†] khorramiana@semnan.ac.ir
[‡] spaktinat@yazd.ac.ir

By utilizing more powerful particle accelerators such as the LHC and Tevatron, we have access to the data that belong to various processes such as top-quark and jet production, and at different center-of-mass energies. New experimental data provide an opportunity to additionally improve the structure of the hadrons which are described by PDFs.

Deep inelastic scattering (DIS) experimental data from the electron (positron)-proton ($e^{\pm}p$) collider and in fixed-target experiments at HERA [5] have allowed us to obtain precise, valuable information about PDFs at small values of x. In spite of this, these data provide no useful constraint on the gluon PDF at large x, which is relevant for phenomenological applications at hadron-hadron colliders such as the LHC and Tevatron. In the present analysis, the DIS final inclusive HERA combined cross-section data [5] can be considered as base and common data.

In addition to this kind of data as a base dataset, other supplementary processes are also employed for PDF extraction. The final heavy flavor and HERA jet cross-section data [35–42] provide detailed information on PDFs, especially for gluon distributions at low values of x, and they help to constrain the strange PDF in the proton. Although heavier target data are available, in order to avoid any influence of nuclear correction uncertainties, these data in QCD analysis are not used by some groups.

The precision measurements on jet production from high-energy pp and $p\bar{p}$ scattering [43–47] are also necessary for PDF QCD analysis. These data have provided complementary information on the nucleons' flavor structure. Also, they are important in detailed PDF validations in order to reduce their uncertainties and the value of strong coupling constant determination.

To improve the gluon PDF situation with large x, in addition to the above mentioned datasets commonly used to constrain PDFs, certain complementary processes such as top-quark cross-section data [48–58] may also be considered. Such data have a good potential to constrain some PDFs at large values of x [59]. Our motivation to include this kind of data in our analysis is that the gluon PDF is one of the poorly known PDFs in the proton, particularly for $x > 0.3$. In Fig. 1, the NLO and next-to-next-to-leading-order (NNLO) gluon PDF ratios of the HERA [7], MSHT20 [8], NNPDF [9], and PDF4LHC [10] predictions to the CT18 data [6] are compared. In this figure, one can see the sizable difference between these extracted results for large x values. So, in the present study, we have enough motivation to provide a PDF set in the presence of top-quark pair production and jet measurements extracted from hadron-hadron collisions to find the impact of this kind of data on the central value and relative uncertainties of PDFs, especially the gluon PDF at large values of x and the values of the strong coupling constant. In particular, this kind of data allows us to reduce the uncertainties in the gluon PDF at a GeV scale, especially for large x values, as well as in the strong coupling constant.

Although the main motivation of our present study is to focus on the gluon PDF and its uncertainty at large x, we note that the heavy PDF behavior in this region is also very important. As we will see, the accuracy of the charm PDF and its uncertainty benefit from an accurate gluon determination and also the decrease of its uncertainty at large x. On the theoretical side, this may be very worthwhile when one needs to add the charm PDF (or extrinsic charm) to the intrinsic charm (IC) which is dominant at large x. We refer the reader to Refs. [60,61], and references therein for a detailed discussion of the Brodsky, Hoyer, Peterson, and Sakai (BHPS) model. An important review of the intrinsic heavy PDF content of the proton has been published in Ref. [62]. Several phenomenological and theoretical studies have been reported using an IC component in the proton [63–74]. In Refs. [75,76], the intrinsic light-quark sea in the proton using the BHPS model is also studied. A method to generate the intrinsic charm and bottom content of the proton is presented in Ref. [77]. Also, a study of heavy flavor and Higgs production from intrinsic charm and bottom quarks is presented in Ref. [78]. Recently, new

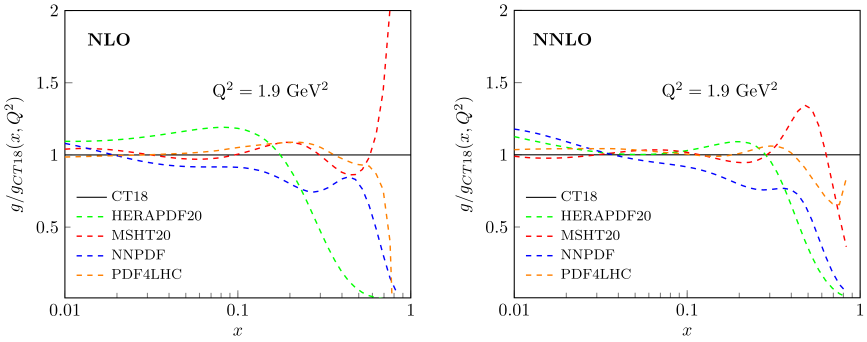

FIG. 1. Gluon PDF ratios of the NLO (left) and NNLO (right) HERAPDF20 [7], MSHT20 [8], NNPDF [9] and PDF4LHC [10] predictions to the CT18 [6] ones, $g/g_{\mathrm{CT18}}(x,Q^2)$ as a function of x at $Q^2 = 1.9\ \mathrm{GeV}^2$.

constraints on the IC contribution using the BHPS approach with the determination of $\alpha_s(M_Z^2)$ and $P_{c\bar{c}/p}$ IC probability values has been reported in Ref. [18]. Note that the $c(x)$ and $\bar{c}(x)$ functions from intrinsic charm are very different. This has very strong consequences for experiments at large x. This is in marked contrast to the Dokshitser-Gribov-Lipatov-Altarelli-Parisi (DGLAP) and perturbative $g \to c + \bar{c}$ symmetric distributions. In Ref. [79], the first lattice QCD calculation of the charm-quark contribution to study the constraints on the charm asymmetry $c(x) \neq \bar{c}(x)$ in the nucleon from lattice gauge theory is presented.

In order to perform an accurate theoretical description, both the PDF evolution and the cross sections of hard scattering are necessary. For PDF evolution, open source codes such as QCDNUM [80] and QCD Pegasus [81] are available in x and Mellin N-space, respectively. To use the hard scattering cross sections of the different processes, different methods such as APPLGrid [82], FastNLO [83], and HATHOR [84] have been developed. Some groups have also reported their open source code for the theory predictions of the cross sections which are used in their analyses. The xFitter [85] computational framework, previously known as HERAfitter [86], as an open source package, provides a framework for PDF determination. In particular, xFitter enables the choice of theoretical options to extract the PDF-dependent cross-section predictions and allows for a choice of different schemes for heavy PDFs. In our QCD analysis, we use the xFitter computational framework. In Refs. [18,87,88], xFitter is used to extract the PDFs and the value of the strong coupling constant. Note that the determination of the strong coupling constant at NLO and NNLO concurrently with the parton distribution function is one of the main purposes of this paper.

The outline of this paper is as follows: In Sec. II, we briefly discuss the experimental measurements used to constrain PDFs and stress the need to include only the necessary datasets in our analysis. In this section also, all datasets, such as base, non-LHC, and LHC data, which are included in the fit procedures, are explained. The theoretical frameworks, computational setting, and PDF parametrization utilized in the present analysis are described in Sec. III. In Sec. IV, we present and interpret the results of the fits and the impact of the different measurements on PDFs using different fits. The PDFs extracted from different fits are correlated with the strong coupling constant; therefore, it is an important parameter to be determined with the PDFs simultaneously. In addition, the reduction of gluon and charm PDF uncertainties at large x as the most prominent case, the determination of total charm PDFs considering the BHPS model, and the Higgs boson cross-section prediction to address PDF uncertainties are illustrated in Sec. IV. Finally, our conclusion and discussion are given in Sec. V.

II. DESCRIPTION OF EXPERIMENTAL MEASUREMENTS FOR PDF ANALYSIS

Basically, a broad set of hard scattering cross sections from DIS pp and $p\bar{p}$ collisions, which provide the PDF information over a wide range of x and Q^2 and for different flavor combinations, are used in this PDF QCD analysis. While the common PDF fits were based mostly on the DIS process, in recent years other measurements and processes such as heavy flavor, inclusive jet, and also top-quark cross sections have had a very important impact for constraining the PDFs [6–9].

To have a precise constraint for all the PDFs in a wide region of x and Q^2 (and not in just a special region), we need to perform a PDF analysis using a completely global fit, including as many data as possible.

One of the datasets which we may include in a PDF analysis is the fixed-target DIS data collected by some experiments (such as SLAC, BCDMS, NMC, etc.) with proton and deuteron targets. These kinds of data are sensitive to some PDFs in specific regions. To add the fixed-target DIS data in a completely global fit, we have to add some additional parameters in some parton distribution due to the kinematic region of these data (low values of Q^2) to have a better agreement in QCD fits. Another point is that the deuterium DIS data necessitate considering the differences between PDFs in the deuteron and those in the free proton and neutron. It is obvious that including fixed-target DIS data in the presence of all other datasets, which will be introduced in this section, has an impact on some PDFs, especially valence PDFs, and consequently, it may impact on the gluon PDF at large x via DGLAP evolution. We find that the gluon PDF will be somewhat different at low x by including and excluding the fixed-target DIS data in the presence of all other datasets in the present analysis.

As we mentioned before, in order to focus on datasets with an impact on the high-x gluon, although heavier target data are available, to avoid any influence of nuclear correction uncertainties and to add some additional parameters, these kinds of data are not used in the present analysis.

Although the impact of particular datasets on a particular PDF, such as the gluon PDF in a wide region of x and Q^2, can only truly be assessed in a completely global fit, a study such as this analysis can give us some idea about the impact of particular datasets on some PDFs, especially the gluon PDF at large x.

In this analysis, we determine PDFs by including a selection of datasets (1891 data points) from the combined HERA I + II deep-inelastic scattering data along with other

TABLE I. The list of all datasets: DIS HERA I + II, non-LHC, and LHC data used in the present analysis. For each dataset, we indicate the process, measurement, reference, and the ranges of their kinematic cuts such as x, y, Q^2 [GeV^2], p_T [GeV], E_T [GeV], $\sqrt{s}$ [TeV], and $\mathcal{L}$ [fb^{-1}].

Dataset	Process	Experiment	Ref.	Kinematic ranges and details	
HERA I + II					
DIS σ	$e^{\pm}p \to \overset{\nu}{(-)}X$	HERA I + II CC $e^{+}p$	[5]	$3\times10^{2} \le Q^{2} \le 3\times10^{4}$,	$8.0\times10^{-3} \le x \le 0.4$
		HERA I + II CC $e^{-}p$	[5]	$3\times10^{2} \le Q^{2} \le 3\times10^{4}$,	$8.0\times10^{-3} \le x \le 0.65$
	$e^{\pm}p \to e^{\pm}X$	HERA I + II NC $e^{-}p$	[5]	$60 \le Q^{2} \le 5\times10^{4}$,	$8.0\times10^{-4} \le x \le 0.65$
		HERA I + II NC $e^{-}p$ 460	[5]	$6.5 \le Q^{2} \le 8\times10^{2}$,	$3.48\times10^{-5} \le x \le 0.65$
		HERA I + II NC $e^{-}p$ 575	[5]	$6.5 \le Q^{2} \le 8\times10^{2}$,	$3.48\times10^{-5} \le x \le 0.65$
		HERA I + II NC $e^{+}p$ 820	[5]	$6.5 \le Q^{2} \le 3\times10^{4}$,	$6.21\times10^{-7} \le x \le 0.4$
		HERA I + II NC $e^{+}p$ 920	[5]	$6.5 \le Q^{2} \le 3\times10^{4}$,	$5.02\times10^{-6} \le x \le 0.65$
Non-LHC					
DIS heavy quarks	$e^{\pm}p \to e^{\pm}cX$	H1-ZEUS Charm	[42]	$2.5 \le Q^{2} \le 2\times10^{3}$,	$1\times10^{-3} \le x \le 5\times10^{-2}$
	$e^{\pm}p \to e^{\pm}bX$	H1-ZEUS Beauty	[42]	$2.5 \le Q^{2} \le 2\times10^{3}$,	$3\times10^{-5} \le x \le 5\times10^{-2}$
	$e^{\pm}p \to jX$	H1 65.4 pb^{-1}	[38]	$1.5\times10^{2} \le Q^{2} \le 1.5\times10^{4}$,	$7 \le E_T \le 50$
		H1 395 pb^{-1}	[39]	$1.5\times10^{2} \le Q^{2} \le 1.5\times10^{4}$,	$7 \le p_T \le 50$
		H1 43.5 pb^{-1}	[40]	$5 \le Q^{2} \le 10^{2}$,	$5 \le p_T \le 80$
		H1 351 pb^{-1}	[41]	$1.5\times10^{2} \le Q^{2} \le 1.5\times10^{4}$,	$7 \le p_T \le 50$
Lepton-hadron jet	$e^{\pm}p \to 2jX$	H1 dijets	[41]	$1.5\times10^{2} \le Q^{2} \le 1.5\times10^{4}$,	$5 \le p_T \le 50$
	$e^{\pm}p \to 3jX$	H1 trijets	[41]	$1.5\times10^{2} \le Q^{2} \le 1.5\times10^{4}$,	$5 \le p_T \le 50$
		ZEUS 300 GeV	[35]	$1.25\times10^{2} \le Q^{2} \le 10^{4}$,	$8 \le E_T \le 100$
	$e^{\pm}p \to jX$	ZEUS 318 GeV	[36]	$1.25\times10^{2} \le Q^{2} \le 10^{4}$,	$8 \le E_T \le 100$
	$e^{\pm}p \to 2jX$	ZEUS dijet	[37]	$1.25\times10^{2} \le Q^{2} \le 2\times10^{4}$,	$8 \le E_T \le 60$
Hadron-hadron jet	$hh \to jX$	CDF	[46]	$6.2\times10 \le p_T \le 7\times10^{2}$,	$\lvert y\rvert \le 2.1$
		DØ	[47]	$5\times10 \le p_T \le 6\times10^{2}$,	$\lvert y\rvert \le 2.4$
Hadron-hadron top	$hh \to t\bar{t}$	DØ-CDF (total)	[48]	$\sqrt{s} = 1.96$,	$\mathcal{L} = 8.8$
		DØ (total)	[49]	$\sqrt{s} = 1.8$,	$\mathcal{L} = 1.1\times10^{5}$
LHC					
Hadron-hadron jet	$hh \to jX$	CMS	[43]	$7.4\times10 \le p_T \le 2.5\times10^{3}$,	$\lvert y\rvert \le 3.0$
		ATLAS	[44]	$2\times10 \le p_T \le 4.3\times10^{2}$,	$\lvert y\rvert \le 0.4$
		ATLAS	[45]	$2\times10 \le p_T \le 1.5\times10^{3}$,	$\lvert y\rvert \le 4.4$
Hadron-hadron top	$hh \to t\bar{t}$	CMS (total)	[50–53]	$5.02 \le \sqrt{s} \le 13$,	$5 \le \mathcal{L} \le 3.04\times10^{5}$
		CMS (differential)	[54]	$\sqrt{s} = 7$,	$0 \le p_T \le 400$
		ATLAS (total)	[55–57]	$5.02 \le \sqrt{s} \le 13$,	$3.2 \le \mathcal{L} \le 2.57\times10^{5}$
		ATLAS (differential)	[58]	$\sqrt{s} = 7$,	$0 \le p_T \le 350$

non-LHC and LHC data. The various PDF fits are performed on three different datasets: (i) inclusive HERA I + II cross-section data as a base input dataset, (ii) non-LHC data, (iii) LHC data. In this section, an overview is presented of the currently available experimental measurements reported by various collaborations that are included in our fit procedures. In the following subsections, the type of reaction, the ranges of kinematic variables for all datasets, and the role of these experimental measurements in the extraction of parton distribution functions and the strong coupling constant are mentioned. The details of the utilized experimental data are explained in Tables I–III.

A. Inclusive HERA I + II cross sections

In this subsection, we discuss the significant role of final HERA I + II data, since these data have improved constraints on small-x sea quarks and gluon PDFs.

We use neutral- and charged-current combined final HERA run I + II data [5] with a variety of beam energies. The H1 and ZEUS Collaborations at HERA reported a combination of inclusive deep inelastic $e^{\pm}p$ scattering cross sections for neutral- and charged-current interactions. The energies of proton beams are 460, 575, 820, and 920 GeV, and the energies of both $e^{\pm}$ beams are 27.5 GeV. The corresponding center-of-mass energies

TABLE II. The recent measurements of top-quark pair production total cross sections in different center-of-mass energies ($\sqrt{s}$) and integrated luminosities ($\mathcal{L}$) with corresponding uncertainties, reported by the DØ and CDF collaborations at Fermilab, and the ATLAS and CMS collaborations at LHC.

$\sqrt{s}$ [TeV]	$\mathcal{L}$ [fb^{-1}]	Ref.	$\sigma^{\text{tot}}_{\text{Exp}}(t\bar{t})$ [pb]
DØ and CDF experiments at Fermilab			
1.96	8.8	[48]	7.60 ± 0.41
1.8	1.1×10^5	[49]	$5.9 \pm 1.2(\text{stat}) \pm 1.1(\text{syst})$
CMS experiments at LHC			
5.02	3.04×10^5	[53]	$60.3 \pm 5.0(\text{stat}) \pm 2.8(\text{syst}) \pm 0.9(\text{lumi})$
7	5	[51]	$173.6 \pm 2.1(\text{stat})\ {}^{+4.5}_{-4}(\text{syst}) \pm 3.8(\text{lumi})$
7	5	[50]	$161.7 \pm 6(\text{stat}) \pm 12(\text{syst}) \pm 3.6(\text{lumi})$
8	19.6	[50]	$227.4 \pm 3.8(\text{stat}) \pm 13.7(\text{syst}) \pm 6(\text{lumi})$
8	19.7	[51]	$244.9 \pm 1.4(\text{stat})\ {}^{+6.3}_{-5.5}(\text{syst}) \pm 6.4(\text{lumi})$
13	35.9	[52]	$803 \pm 2(\text{stat}) \pm 25(\text{syst}) \pm 20(\text{lumi})$
ATLAS experiments at LHC			
5.02	2.57×10^5	[55]	$66.0 \pm 4.5(\text{stat}) \pm 1.6(\text{syst}) \pm 1.2(\text{lumi}) \pm 0.2(\text{beam})$
7	3.2	[56]	$183 \pm 3(\text{stat}) \pm 4(\text{syst}) \pm 4(\text{lumi}) \pm 3(\text{beam})$
8	3.2	[56]	$243 \pm 2(\text{stat}) \pm 5(\text{syst}) \pm 5(\text{lumi}) \pm 4(\text{beam})$
8	20.2	[57]	$248.3 \pm 0.7(\text{stat}) \pm 13.4(\text{syst}) \pm 4.7(\text{lumi})$
13	3.2	[56]	$818 \pm 8(\text{stat}) \pm 27(\text{syst}) \pm 19(\text{lumi}) \pm 12(\text{beam})$

TABLE III. Normalized differential cross sections for $t\bar{t}$ production as a function of p_T, reported by the CMS and ATLAS collaborations [54,58]. The statistical and systematic uncertainties are also shown.

p_T [GeV]	$1/\sigma d\sigma/dp_T$ [GeV^{-1}]	Stat. [%]	Sys. [%]
CMS experiment			
0 to 60	4.54×10^{-3}	±2.5	±3.6
60 to 100	6.66×10^{-3}	±2.4	±4.9
100 to 150	4.74×10^{-3}	±2.4	±3.2
150 to 200	2.50×10^{-3}	±2.6	±5.1
200 to 260	1.04×10^{-3}	±2.9	±5.5
260 to 320	0.38×10^{-3}	±3.7	±8.2
320 to 400	0.12×10^{-3}	±5.8	±9.5
ATLAS experiment			
0 to 50	3.4×10^{-3}	±2.4	±5.1
50 to 100	6.7×10^{-3}	±1.2	±1.9
100 to 150	5.3×10^{-3}	±2.5	±2.6
150 to 200	2.6×10^{-3}	±2.0	±4.8
200 to 250	1.12×10^{-3}	±2.4	±4.8
250 to 350	0.32×10^{-3}	±3.5	±5.5

related to each proton beam are approximately 225, 251, 300, and 320 GeV, and the value of integrated luminosity is about 1 fb^{-1}. These experimental results are available as a function of Q^2 and x. The ranges of these quantities are $0.045 \leq Q^2 \leq 50000$ and $6 \times 10^{-7} \leq x \leq 0.65$ for neutral-current (NC) interactions, and $200 \leq Q^2 \leq 50000$ and $1.3 \times 10^{-2} \leq x \leq 0.40$ for charged current (CC). The inclusive HERA I + II cross-section data are included as a base dataset in our analysis to determine PDFs and the strong coupling constant. For this kind of dataset, we use the kinematic cut $Q^2 > 6.5\ \text{GeV}^2$, which is necessary to remove the higher-twist terms effectively.

B. Non-LHC experimental data

In this part, we introduce the non-LHC dataset which we use in the present analysis. In QCD fits to inclusive HERA I + II data only, the shape of the gluon PDF depends on the value of strong coupling $\alpha_s(M_Z^2)$. In fact, the uncertainty on the gluon PDF is increased for fits with free $\alpha_s(M_Z^2)$ compared to fits with fixed $\alpha_s(M_Z^2)$ [5]. In this regard, in addition to HERA I + II inclusive data, we include the DIS heavy-quark production measurements by the H1 and ZEUS Collaborations at HERA [42]. These kinds of data were proven to be consistent with the inclusive data and also provide a constraint on sea and gluon PDFs at low x at NLO and NNLO [5].

On the other hand, it would be worthwhile to give attention to including experimental data on the jet production cross section in PDF fits, because this kind of data provides an independent measurement of the gluon PDF. These data are also sensitive to $\alpha_s(M_Z^2)$, to gluon PDFs at low Q^2, and to valence PDFs at high Q^2. So, not only do the jet data reduce the uncertainty on high-x gluon PDF with fixed $\alpha_s(M_Z^2)$ in the fits, but they also allow us to determine gluon PDF and accurate $\alpha_s(M_Z^2)$ simultaneously.

We choose H1 and ZEUS jet data [35–41] in the non-LHC dataset.

Finally, in addition to the data mentioned above, other measurements which are also sensitive to PDF determination and strong coupling constant values, such as DØ and CDF data that contain jet experimental measurements [46,47] and top-quark cross sections [48,49], are included.

In the following, we present the details of the non-LHC dataset: heavy-quark production cross sections [42], the H1 and ZEUS jet data [35–41], DØ and CDF data that contain top-quark cross sections [48,49], and jet experimental measurements [46,47], which are added to the DIS HERA data [5] as a base set.

(i) *Heavy flavor HERA cross sections:* In addition to the HERA I + II inclusive combination which we mentioned in the previous subsection, the combined measurements of charm- and beauty-quark cross sections reported by the H1 and ZEUS Collaborations [42] are also available in the kinematic ranges of $2.5 < Q^2 < 2000\ \mathrm{GeV}^2$ and $3 \times 10^{-5} < x < 5 \times 10^{-2}$. Taking into account the heavy-quark cross-section data in a PDF fit will cause restrictions on the gluon distribution [42], and it is also valuable for obtaining the strong coupling constant value [5].

(ii) *H1 jet cross sections:* Four different jet cross-section experimental measurements [38–41] reported by the H1 Collaboration are included in our analysis for extracting PDFs. These jet cross-section measurements play a significant role in processes for determining the strong coupling constant.

The first inclusive jet cross section [38] is neutral-current deep-inelastic e^+p scattering with center-of-mass energy and integrated luminosity values of 319 GeV and 65.4 pb^{-1}, respectively. The jet cross sections are measured as a function of Q^2 and transverse energy (E_T) with the ranges $150 \leq Q^2 \leq 15000\ \mathrm{GeV}^2$ and $7 \leq E_T \leq 50$ GeV.

The second set of H1-inclusive jet cross-section experimental data [39] is from the electron-proton DIS neutral-current process, reported at $\sqrt{s} = 319$ GeV, and the related integrated luminosity of the experiment is equal to 395 pb^{-1}. The inclusive jet cross sections are functions of Q^2 and transverse momentum covering the ranges $150 \leq Q^2 \leq 15000\ \mathrm{GeV}^2$ and $7 \leq p_T \leq 50$.

The third set of H1-inclusive jet cross-section data [40] extracted from positron-proton deep inelastic scattering corresponds to center-of-mass energy and integrated luminosity values of 319 GeV and 43.5 pb^{-1}, respectively. The jet experimental data are reported as a functions of Q^2 and jet transverse momentum with the ranges $5 \leq Q^2 \leq 100\ \mathrm{GeV}^2$ and $5 \leq p_T \leq 80$ GeV.

The fourth and last set of H1 experimental data [41] included consists of the inclusive jet, dijet, and trijet double-differential cross sections. The mentioned cross sections are measured in neutral-current deep inelastic electron-proton scattering. The center-of-mass energy is equal to 319 GeV, and the value of the integrated luminosity is 351 pb^{-1}. The inclusive jet cross-section data are reported as functions of $150 \leq Q^2 \leq 15000$ and $7 \leq p_T \leq 50$. The dijet and trijet double-differential cross sections are reported as a functions of Q^2 and transverse momentum, such that the range of this variable for both dijet and trijet data is $5 \leq p_T \leq 50$ GeV.

According to fit results in the literature, all inclusive jet cross sections are important in particular for determining the value of the strong coupling constant [38–41].

(iii) *ZEUS jet cross sections:* Three different jet experimental measurements reported by the ZEUS Collaboration [35–37] are used in our PDF fit. In the following, the properties of these measurements are explained.

The first measurement is the inclusive jet differential cross section [35] related to neutral-current deep inelastic positron-proton scattering with a center-of-mass energy of 300 GeV, where the Q^2 of virtual bosons is larger than 125 GeV^2, and the value of integrated luminosity related to this experiment is 38.6 pb^{-1}. These experimental data are presented as functions of jet transverse energy, jet pseudorapidity, and Q^2, where the range of jet transverse energy is $8 \leq E_T \leq 100$ GeV and the range of the jet pseudorapidity variable is from −2 to 1.8. The described jet cross-section data are important in processes for determining the strong coupling constant [35].

The second inclusive jet cross-section measurement presented by the ZEUS Collaboration [36] is reported at a center-of-mass energy of 318 GeV and with an integrated luminosity of 82 pb^{-1}. The inclusive jet cross sections are measured in NC deep inelastic electron-proton scattering. These measurements are presented as functions of transverse energy and Q^2 with the ranges $8 \leq E_T \leq 100$ GeV and $1.25 \times 10^2 \leq Q^2 \leq 10^4\ \mathrm{GeV}^2$, respectively [36]. In particular, in a global fit, these data are able to constrain the gluon density [36].

The third and last set of ZEUS experimental data [37] that is included in fits of present QCD analysis is from inclusive dijet cross-section measurements. The values of the center-of-mass energy and integrated luminosity of the experiment are 319 GeV and 374 pb^{-1}, respectively. The dijet cross sections are reported as a function of Q^2 and the jet transverse energy, with the ranges of $125 \leq Q^2 \leq 20000\ \mathrm{GeV}^2$ and $8 \leq E_T \leq 60$ GeV, respectively. Also, the invariant mass of the mentioned dijet system is larger than 20 GeV. In a fit procedure, these dijet data have the potential to improve the gluon uncertainty in the high-x region particularly, and in addition are important for determining the value of the strong coupling constant [37].

(iv) *CDF jet cross sections:* The measurement of the inclusive jet cross section is reported by the CDF Collaboration [46], using $p\bar{p}$ collisions at the center-of-mass energy of 1.96 TeV with the integrated luminosity of 1.3 fb^{-1}. The measurement is presented as a function of jet rapidity and jet transverse momentum, with the covering ranges of $|y| \leq 2.1$ and $62 \leq p_T \leq 700$ GeV. This experimental dataset in a global fit causes constraints in the high-x regions on PDFs, and particularly on gluon distribution, and can also reduce the gluon uncertainty at high x. It occurs when the measured jet cross sections have the tendency to be lower than the central NLO predictions of perturbative QCD [46].

(v) *DØ jet cross sections:* The inclusive jet cross-section experimental data are reported by the DØ Collaboration [47] from $p\bar{p}$ collisions, as a function of jet rapidity and jet transverse momentum with the ranges of $|y| \leq 2.4$ and $50 \leq p_T \leq 600$ GeV, respectively. The values of the center-of-mass energy and integrated luminosity related to this experiment are 1.96 TeV and 0.7 fb^{-1}, respectively. In research for extracting PDFs by considering these experimental data, constraints on gluon PDFs are highly expected [47,89].

(vi) *Total $t\bar{t}$ Tevatron cross section:* The top-quark total cross-section measurements reported by the DØ and CDF collaborations are also included in the fits. The DØ and CDF total top-quark cross sections [48,49] measured at both 1.8 and 1.96 TeV are included in the fits to extract the PDFs and the strong coupling constant. The details and values of these measurements are summarized in Table II.

C. LHC data

We now present the inclusion of LHC data in our analysis. This includes a variety of data on jet and top-quark cross sections. We will present more details of the fit quality and the PDFs extraction in later sections, but first we present each of the different types of LHC data included in the present fit:

(vii) *CMS and ATLAS jet cross sections:* The experimental measurements of double-differential jet cross sections ($pp \to \mathrm{jets} + X$) are reported by the CMS Collaboration [43] as a function of absolute jet rapidity ($|y| \leq 3.0$) and jet transverse momentum ($74 \leq p_T \leq 2500$ GeV) in the center-of-mass energy of 8 TeV and integrated luminosity of 19.7 fb^{-1}. These experimental high-p_T double-differential jet cross-section measurements can reduce significantly the uncertainties of gluon PDFs and are also important for determining the value of the strong coupling constant [43].

Also, the inclusive jet cross-section data are reported by the ATLAS Collaboration [44], with the center-of-mass energy of 2.76 TeV and integrated luminosity of 0.2 pb^{-1}. These experimental data are presented as a function of jet rapidity $|y| \leq 0.4$ and jet transverse momentum $20 \leq p_T \leq 430$ GeV. On the other hand, the ATLAS [45] jet cross-section measurement at $\sqrt{s} = 7$ TeV and the integrated luminosity of 37 pb^{-1} is included in the fit. These jet cross-section data are a function of jet rapidity ($|y| \leq 4.4$) and jet transverse momentum ($20 \leq p_T \leq 1500$ GeV). The above mentioned ATLAS jet cross-section data are able to provide an important impact on gluon and sea-quark distributions in the high-x region [44].

(viii) *Top-quark cross sections:* The top-quark cross-section measurements reported by ATLAS and CMS are also included in the present analysis. The CMS top-quark data containing the differential cross sections are reported at the center-of-mass energy of 7 TeV as a function of transverse momentum (p_T) [54]. The CMS top-quark total cross sections are measured at various center-of-mass energies such as 5.02, 7, 8, and 13 TeV [50–53]. The ATLAS differential cross-section data [58] at the center-of-mass energy 7 TeV and the top-quark total cross-section measurements [55–57] at the center-of-mass energies of 5.02, 7, 8, and 13 TeV are also included in the final PDF fit. The details of these measurements are summarized in Tables II and III. According to the reported results in Ref. [90], the top-quark cross-section experimental data are able to create significant constraints on the gluon PDF.

We will see, choosing the complete dataset as we show in Table I, including LHC data along with the combined HERA and non-LHC dataset in the current analysis, the LHC data will impact on gluon and charm PDF uncertainties at high x significantly, in respect to the fit of HERA data only and HERA with non-LHC datasets.

III. THEORETICAL FRAMEWORK

As previously mentioned, various types of experimental data such as HEAR I + II, non-LHC, and LHC data are included in our fit procedures. In the following section, the most important computational aspects, such as PDF parametrization and the minimization method, which are considered for extracting PDF sets are explained.

The present QCD analysis for PDF determination is performed in the xFitter framework. The xFitter package [85], an updated version of HERAfitter [86], is used to extract PDFs and the strong coupling constant with the main advantage of utilizing several computational programs simultaneously.

To perform a global fit, Dokshitser-Gribov-Lipatov-Altarelli-Parisi [91–93] evolution equations derive PDFs at any scale relevant to comparisons with the experimental data from the parametrization of PDFs at an input scale of Q_0^2. For preparing the NLO and NNLO numerical solutions of DGLAP evolution equations of PDFs at higher scales $Q^2 > Q_0^2$, the QCDNUM [80] package is utilized. In this regard, the parametric forms for the PDF, $xf(x, Q_0^2)$ at the lower scale of QCD evolution, are needed.

To include the heavy-quark contribution to any process, it is necessary to apply the variable flavor-number scheme (VFNS), so that the different numbers of active flavors (N_f) are adopted at different Q^2 scales. In this regard, the Thorne-Roberts variable flavor-number scheme [94] is used to calculate the contributions of the heavy quarks. Very recently the three–loop Wilson coefficients have been calculated in Ref. [95].

The jet cross-section data reported by ATLAS and CMS collaborations are available to include in the xFitter framework. To include the jet experimental cross-section data, the APPLGrid [82] and FastNLO [83] computational programs may be used in the fit procedures. The grid file of ATLAS jet cross sections is obtained by APPLGrid, and the grid file of the CMS jet cross section is available by the FastNLO computational package. Since the ATLAS jet cross-section grid files are not available at NNLO, using k-factor technique is necessary in order to include these experimental data at NNLO. The HATHOR [84] and FastNLO computational packages are also used to include the total and differential top-quark cross sections. Finally, the MINUIT [96] program is used for the minimization.

In this analysis, the minimum cut value which is implied on HERA I + II data is $Q^2_{\rm min} = 6.5\ \mathrm{GeV}^2$, with the invariant mass squared of $W^2 > 15\ \mathrm{GeV}^2$. We did not apply any other cuts in this analysis. The value of the initial QCD scale is assumed to be $Q_0^2 = 1.9\ \mathrm{GeV}^2$, which is below the c-quark mass threshold. The masses of heavy quarks [7] are considered to be $m_c = 1.43$ GeV, $m_b = 4.5$ GeV, and $m_t = 173.5$ GeV.

The PDFs at the initial scale are represented by the following general form:

$$xf_i(x, Q_0^2) = A_i x^{B_i}(1-x)^{C_i}(1 + D_i x + E_i x^2), \quad (1)$$

where i indicates the flavor of the parton distribution, and for each PDF flavor combination the parameters of the PDF shape are different. The x^{B_i} term affects the low-x PDF behavior, and the $(1-x)^{C_i}$ term ensures that the parton distribution disappears in the $x \to 1$ elastic limit. Also, the last term in Eq. (1) controls the behavior of the PDFs away from the extrapolation regions of $x \to 0$ and $x \to 1$. The normalization parameters A_i can be determined via QCD sum rules.

The parametrized parton distributions, xf_i, are chosen to be the valence, light sea, and gluon PDFs. The detailed parametrizations for each PDF at the initial scale are as follows [44]:

$$\begin{aligned}
xu_v(x, Q_0^2) &= A_{u_v} x^{B_{u_v}}(1-x)^{C_{u_v}}(1 + E_{u_v} x^2),\\
xd_v(x, Q_0^2) &= A_{d_v} x^{B_{d_v}}(1-x)^{C_{d_v}},\\
x\bar{U}(x, Q_0^2) &= A_{\bar{U}} x^{B_{\bar{U}}}(1-x)^{C_{\bar{U}}},\\
x\bar{D}(x, Q_0^2) &= A_{\bar{D}} x^{B_{\bar{D}}}(1-x)^{C_{\bar{D}}},\\
xg(x, Q_0^2) &= A_g x^{B_g}(1-x)^{C_g} - A'_g x^{B'_g}(1-x)^{C'_g}. \quad (2)
\end{aligned}$$

Here, xu_v and xd_v are the valence quark distribution, while $x\bar{U}$ and $x\bar{D}$ indicate the u-type and d-type antiquark distributions, respectively, where $x\bar{U} = x\bar{u}$ and $\bar{D} = x\bar{d} + x\bar{s}$, and the gluon distribution is represented by xg.

The QCD sum rules determine the normalization parameters. The parameters A_{u_v}, A_{d_v} are fixed by considering the rule of quark counting, and the A_g parameter is fixed using the momentum sum rule. The relation between $A_{\bar{U}}$ and $A_{\bar{D}}$ is $A_{\bar{U}} = A_{\bar{D}}(1 - f_s)$, and the $B_{\bar{U}}$ and $B_{\bar{D}}$ parameters are considered to be equal, $B_{\bar{U}} = B_{\bar{D}}$. The last two relations are set to guarantee that $x\bar{u} \to x\bar{d}$ as $x \to 0$. The distribution of strange quarks is assumed to be an x-independent fraction (f_s) of the down-type sea, $x\bar{s} = f_s x\bar{D}$, at Q_0^2, and the value of f_s is chosen to be equal to 0.31 [44].

The xg gluon PDF in Eq. (2) is an exception from Eq. (1), with the subtraction of an additional term of the form $A'_g x^{B'_g}(1-x)^{C'_g}$, which makes the parametrization at low x [5] more flexible than a single power and positive values of xg at large x, as suggested in Ref. [89]. Note that as the first term of gluon PDF cannot be controlled by the single power B_g as x approaches zero, we need to consider the second term of the gluon PDF parametrization. It requires that the powers B_g and B'_g be different. This additional term is considered at NLO and NNLO. The C'_g parameter is fixed to 25 for all fit procedures of this QCD analysis.

The χ^2 function described here is a criterion to find out how a QCD model can be compatible with the experimental measurements. In this analysis, we extract the best values of 14 independent free parameters by minimizing the χ^2 function. In cases where all of the correlated uncertainties related to experimental measurements are available, the χ^2 function, as implemented in the xFitter framework, is given by [97]

$$\chi^2 = \sum_i \frac{[d_i - t_i(1 - \sum_j \beta^i_j s_j)]^2}{\delta^2_{i,unc} t_i^2 + \delta^2_{i,\mathrm{stat}} d_i t_i} + \sum_j s_j^2. \qquad (3)$$

Here, t_i and d_i are theoretical predictions and experimental measurements of the ith data point, respectively. Also, β^i_j are the corresponding systematic uncertainties, and s_j are the nuisance parameters associated with the correlated systematic uncertainties, and j indicates sources of correlated systematic uncertainties. In the above equation, $\delta^2_{i,\mathrm{stat}}$ and $\delta^2_{i,unc}$ indicate relative statistical and uncorrelated systematic uncertainties. The MINUIT [96] package is used for minimizing the χ^2 function in the xFitter framework.

Determination of the uncertainty of free parameters is also very worthwhile in addition to extracting the central values of these parameters. The uncertainties of parton distribution functions are estimated in Refs. [98–106]. One of the most important approaches is the Hessian method. Although the details of this method are presented in these references, due to utilizing it in the present QCD analysis, a review of the Hessian method is described.

According to the Hessian approach, by considering ζ_i ($i = 1, 2, \ldots, N$) as free parameters, where N is the number of parameters which are extracted from the fit procedure, the χ^2 function can expand around the minimum χ^2 point $\hat{\zeta}$:

$$\Delta\chi^2(\zeta) = \chi^2(\hat{\zeta} + \delta\zeta) - \chi^2(\hat{\zeta}) = \sum_{i,j} H_{ij}\delta\zeta_i\delta\zeta_j. \qquad (4)$$

Here, just the leading quadratic term is considered, and H_{ij} denotes the second Hessian derivative matrix. The confidence region is expressed by assigning a value to $\Delta\chi^2$ in the parameter space.

If the number of parameters is 1 (i.e., $N = 1$), the confidence level is 68% for $\Delta\chi^2 = 1$. Generally, in the case of $N \neq 1$, the value of $\Delta\chi^2$ should be changed. It is known that the confidence level P is related to the number of parameters and $\Delta\chi^2$ as follows:

$$P = \int_0^{\Delta\chi^2} \frac{1}{2\Gamma(N/2)} \left(\frac{\omega}{2}\right)^{(\frac{N}{2})-1} \exp\left(-\frac{\omega}{2}\right) d\omega. \qquad (5)$$

Here, $\Gamma(N/2)$ is the well-known gamma function. The standard confidence level $P = 0.6826$ corresponds to a 1σ error range [104–106]. The $\Delta\chi^2$ value is numerically calculated by choosing a confidence level value using Eq. (5). In the present analysis, we have $N = 14$, and by supposing the confidence level to be $P = 0.6826$, the consequent value of $\Delta\chi^2$ will be 15.94. By running the MINUIT subroutine [96], the Hessian matrix is made available.

The uncertainty of a certain observable ($\mathcal{O}$), which is introduced at the input scale Q_0^2, can be reached by the Hessian method. By using the $\Delta\chi^2$ value and derivatives of the observables with respect of the free parameters, the uncertainties for a given observable ($\mathcal{O}$) are calculable:

$$[\delta\mathcal{O}_i]^2 = \Delta\chi^2 \sum_{j,k} \left(\frac{\partial\mathcal{O}_i(\zeta)}{\partial\zeta_j}\right)_{\hat{\zeta}} H^{-1}_{jk} \left(\frac{\partial\mathcal{O}_i(\zeta)}{\partial\zeta_k}\right)_{\hat{\zeta}}. \qquad (6)$$

Therefore, using $\Delta\chi^2$ and derivatives of $\mathcal{O}_i$ with respect to extracted parameters (ζ_i), the above equation returns the uncertainty ($\delta\mathcal{O}_i$) of the desired observable. At any other scale of Q^2, the uncertainties can be calculated by evolving obtained gradient terms with the DGLAP evolution kernel [91–93].

IV. FIT RESULTS

To investigate the impact of top-quark and jet cross-section measurements at the LHC on PDFs, in the presence of HERA I + II combined data as a base set, and also non-LHC datasets, we divide our QCD fits into three different fits in the present analysis. The detailed information for each dataset is summarized in Table I. For this purpose, three different fits with the names “Fit A,” “Fit B,” and “Fit C” are introduced below at both NLO and NNLO:

1. *Fit A*: In the first step, we include the DIS HERA I + II combined dataset of Table I, as a base fit, without any additional data. In this fit, we have 1092 data points. Therefore, Fit A provides a proper base for illustrating the impact of additional data on various PDFs and the strong coupling constant.
2. *Fit B*: In the second step, we add the non-LHC experimental data from Table I to Fit A. This is all the same as Fit A, except now all non-LHC data is added to the DIS HERA I + II combined data. In this fit, we have 1555 data points.
3. *Fit C*: As a final fit procedure, we include the LHC data from Table I with Fit B. In this fit, we have 1891 data points, and so this contains the complete analysis.

In all the fits, there are 14 unknown parameters for PDFs and $\alpha_s(M_Z^2)$.

According to Table IV, the extracted value of χ^2/d.o.f. for Fit A is 1.176 and 1.164 at the NLO and NNLO, respectively. These values for Fit B, in which the other additional non-LHC are included, are 1.184 and 1.189 at the NLO and NNLO, respectively. The slight growth at NNLO compared to NLO for Fit B is due to including heavy-quark (charm and beauty) data. The same result has been reported in Ref. [42]. In Fit C, in which we add both

TABLE IV. The numerical results for the correlated χ^2, log penalty χ^2, total χ^2, and the total χ^2/degree of freedom (d.o.f.) of each dataset for Fits A, B, and C at NLO and NNLO.

			χ^2/n points					
			Fit A		Fit B		Fit C	
Observable	Experiment	Ref.	NLO	NNLO	NLO	NNLO	NLO	NNLO
HERA I + II	HERA I + II CC e^+p	[5]	48/39	49/39	66/39	64/39	63/39	62/39
	HERA I + II CC e^-p	[5]	56/42	55/42	53/42	53/42	53/42	54/42
	HERA I + II NC e^-p	[5]	222/159	223/159	235/159	238/159	237/159	239/159
	HERA I + II NC e^+p 820 GeV	[5]	66/66	59/66	64/66	60/66	64/66	59/66
	HERA I + II NC e^+p 920 GeV	[5]	403/348	390/348	411/348	388/348	413/348	389/348
	HERA I + II NC e^-p 460 GeV	[5]	206/195	209/195	206/195	209/195	206/195	209/195
	HERA I + II NC e^-p 575 GeV	[5]	210/243	210/243	212/243	211/243	212/243	210/243
Non-LHC	Charm H1-ZEUS	[42]	⋯	⋯	20/30	25/30	20/30	25/30
	Beauty H1-ZEUS	[42]	⋯	⋯	14/27	23/27	14/27	23/27
	H1 65.4 pb^{-1}	[38]	⋯	⋯	11/24	12/24	11/24	11/24
	H1 395 pb^{-1}	[39]	⋯	⋯	14/24	19/24	14/24	18/24
	H1 43.5 pb^{-1}	[40]	⋯	⋯	18/28	19/28	18/28	20/28
	H1 351 pb^{-1}	[41]	⋯	⋯	25/24	28/24	25/24	28/24
	H1 dijets	[41]	⋯	⋯	42/24	39/24	43/24	38/24
	H1 trijets	[41]	⋯	⋯	9/16	9/16	9/16	10/16
	ZEUS 300 GeV	[35]	⋯	⋯	28/30	30/30	28/30	29/30
	ZEUS 318 GeV	[36]	⋯	⋯	23/30	23/30	23/30	23/30
	ZEUS dijet	[37]	⋯	⋯	16/22	17/22	16/22	16/22
	CDF-Jet	[46]	⋯	⋯	121/72	119/72	128/72	130/72
	DØ-Jet	[47]	⋯	⋯	75/110	82/110	76/110	85/110
	CDF-DØ Combined-Top quark	[48]	⋯	⋯	6/1	2/1	6/1	2/1
	DØ-Top quark	[49]	⋯	⋯	0.33/1	0.1/1	0.25/1	0.1/1
LHC	CMS-Jet	[43]	⋯	⋯	⋯	⋯	141/168	151/168
	ATLAS-Jet 2.76 TeV	[44]	⋯	⋯	⋯	⋯	40/54	41/54
	ATLAS-Jet 7 TeV	[45]	⋯	⋯	⋯	⋯	42/90	44/90
	CMS 7 TeV ($e\mu j$)	[50]	⋯	⋯	⋯	⋯	1/1	0.03/1
	CMS 8 TeV ($e\mu j$)	[50]	⋯	⋯	⋯	⋯	0.63/1	0.03/1
	CMS 7 TeV (bj)	[51]	⋯	⋯	⋯	⋯	0.15/1	0.55/1
	CMS 8 TeV (bj)	[51]	⋯	⋯	⋯	⋯	0.44/1	1/1
	CMS 13 TeV	[52]	⋯	⋯	⋯	⋯	0.48/1	0.07/1
	CMS 5 TeV	[53]	⋯	⋯	⋯	⋯	0.31/1	1/1
	CMS 7 TeV differential	[54]	⋯	⋯	⋯	⋯	23/7	12/7
	ATLAS 5 TeV	[55]	⋯	⋯	⋯	⋯	0.1/1	0.03/1
	ATLAS 7 TeV	[56]	⋯	⋯	⋯	⋯	8/1	3/1
	ATLAS 8 TeV ($Z \to l^+l^-$)	[56]	⋯	⋯	⋯	⋯	0.59/1	0.2/1
	ATLAS 8 TeV (lj)	[57]	⋯	⋯	⋯	⋯	0.34/1	0.22/1
	ATLAS 13 TeV	[56]	⋯	⋯	⋯	⋯	1/1	0.06/1
	ATLAS 7 TeV differential	[58]	⋯	⋯	⋯	⋯	12/6	5/6
Correlated χ^2			66	69	155	170	225	237
Log penalty χ^2			−9.10	−9.29	−0.02	−8.13	+66	+37.00
Total χ^2			1268	1255	1824	1832	2219	2213
Total χ^2/d.o.f.			1268/1078 = 1.176	1255/1078 = 1.164	1824/1541 = 1.184	1832/1541 = 1.189	2219/1877 = 1.182	2213/1877 = 1.179

LHC and non-LHC data to HERA I + II combined data, the extracted NLO and NNLO values of χ^2/d.o.f. are 1.182 and 1.179, respectively. Obviously, in the comparison of NLO and NNLO results for Fit C as a complete fit, there are almost 0.25% improvements for the χ^2 values and the fit quality. Although currently Fit C contains the complete analysis, the comparison of this fit with other fit results would be of interest. According to Table IV, the total χ^2/d.o.f. values at NLO are 1.175, 1.184, and 1.182 for Fits A, B, and C, respectively, considering the DIS

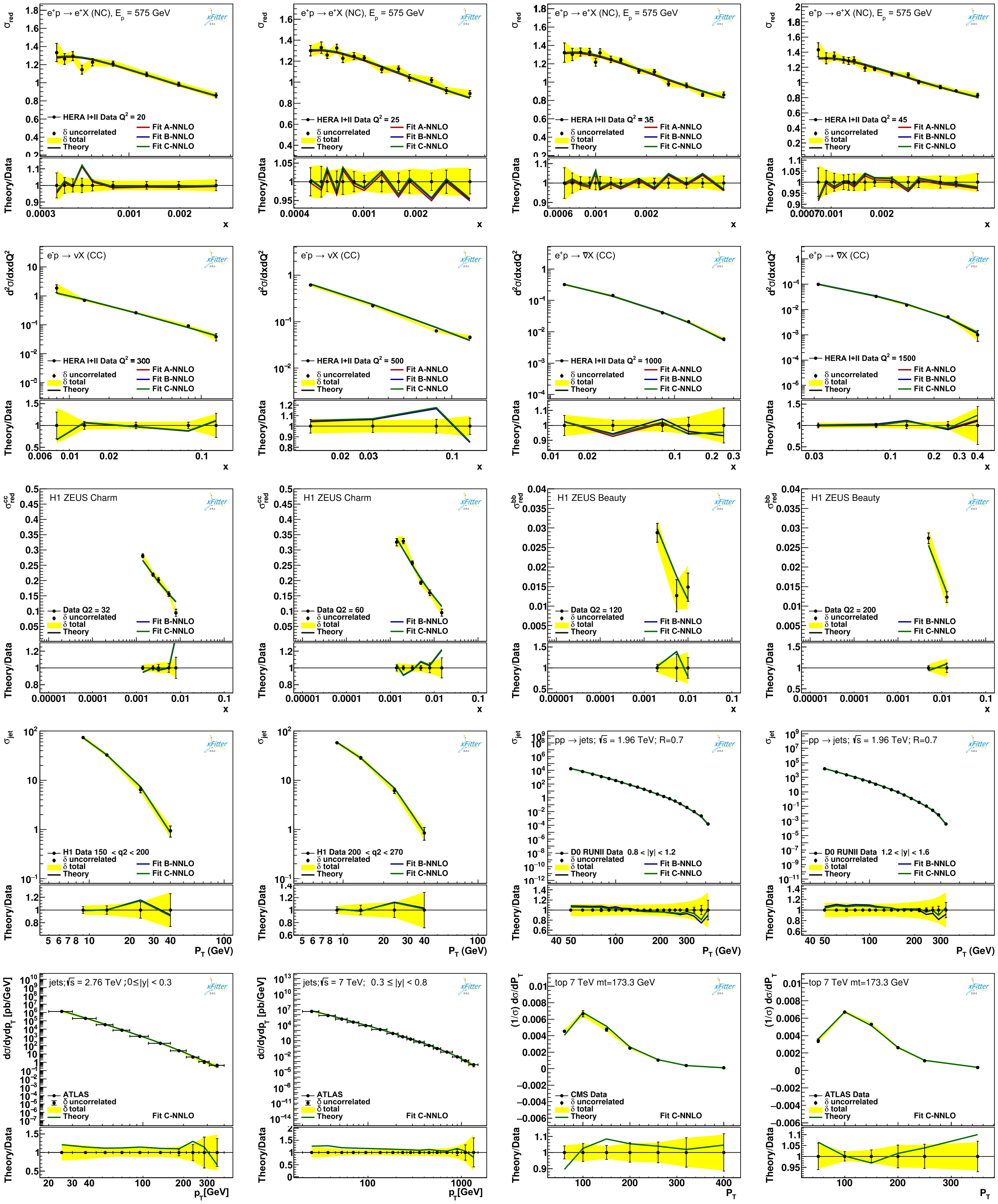

FIG. 2. The results of pQCD calculations for the cross sections of DIS processes, jet production, and the differential cross section of top-quark pair production, and their comparison with experimental measurements.

TABLE V. The numerical values and their uncertainties at the initial scale $Q_0^2 = 1.9\ \mathrm{GeV}^2$ extracted for parameters at NLO and NNLO related to Fits A, B, and C.

	Fit A		Fit B		Fit C	
Parameter	NLO	NNLO	NLO	NNLO	NLO	NNLO
B_{uv}	0.733 ± 0.015	0.731 ± 0.034	0.625 ± 0.016	0.610 ± 0.016	0.644 ± 0.015	0.631 ± 0.014
C_{uv}	4.747 ± 0.047	4.898 ± 0.077	4.887 ± 0.079	4.974 ± 0.072	4.849 ± 0.073	4.982 ± 0.077
E_{uv}	10.10 ± 0.14	11.3 ± 1.5	15.1 ± 1.3	17.9 ± 1.4	13.3 ± 1.2	15.9 ± 1.1
B_{dv}	0.838 ± 0.040	0.869 ± 0.085	0.765 ± 0.061	0.704 ± 0.066	0.796 ± 0.062	0.663 ± 0.060
C_{dv}	4.50 ± 0.14	4.60 ± 0.41	5.08 ± 0.37	4.59 ± 0.38	5.06 ± 0.36	4.13 ± 0.35
$C_{\bar{U}}$	4.14 ± 0.13	5.01 ± 0.69	2.04 ± 0.11	2.065 ± 0.078	1.954 ± 0.061	1.972 ± 0.047
$A_{\bar{D}}$	0.2045 ± 0.0098	0.231 ± 0.014	0.1661 ± 0.0079	0.1784 ± 0.0069	0.1636 ± 0.0070	0.1758 ± 0.0065
$B_{\bar{D}}$	-0.1293 ± 0.0079	-0.1271 ± 0.0091	-0.1582 ± 0.0077	-0.1597 ± 0.0061	-0.1606 ± 0.0070	-0.1624 ± 0.0058
$C_{\bar{D}}$	6.13 ± 0.14	7.7 ± 1.6	4.96 ± 0.75	4.77 ± 0.83	7.4 ± 1.2	5.02 ± 0.80
f_s	0.31 (Fixed)	0.31 (Fixed)	0.31 (Fixed)	0.31 (Fixed)	0.31 (Fixed)	0.31 (Fixed)
B_g	-0.345 ± 0.060	-0.38 ± 0.13	-0.696 ± 0.055	-0.239 ± 0.033	-0.680 ± 0.046	-0.249 ± 0.035
C_g	5.94 ± 0.16	4.9 ± 1.4	2.05 ± 0.30	3.57 ± 0.26	2.27 ± 0.21	4.06 ± 0.20
A'_g	0.790 ± 0.066	0.34 ± 0.20	0.345 ± 0.036	0.096 ± 0.021	0.379 ± 0.030	0.142 ± 0.028
B'_g	-0.419 ± 0.048	-0.526 ± 0.048	-0.709 ± 0.047	-0.582 ± 0.019	-0.696 ± 0.039	-0.546 ± 0.017
C'_g	25.00 (Fixed)	25.00 (Fixed)	25.00 (Fixed)	25.00 (Fixed)	25.00 (Fixed)	25.00 (Fixed)
$\alpha_s(M_Z^2)$	0.1167 ± 0.0014	0.1134 ± 0.0024	0.1198 ± 0.0008	0.1187 ± 0.0007	0.1188 ± 0.0007	0.1179 ± 0.0006

HERA I + II combined, non-LHC, and LHC datasets. These values are 1.164, 1.189, and 1.179 at NNLO. According to Table IV, the NNLO improvement of 1% of $\chi^2/\mathrm{d.o.f.}$ in our base fit (i.e., Fit A) is obtained, with respect to the NLO and NNLO improvements of 0.25% in Fit C, with respect to the NLO. Also, an increase of 0.42% of $\chi^2/\mathrm{d.o.f.}$ is obtained at NNLO with respect to our NLO fit in Fit B.

Our main goal for considering three different fit procedures is investigating the specific impact of various types of cross-section experimental data, such as the HERA I + II combined, non-LHC, and LHC data on PDFs and $\alpha_s(M_Z^2)$ simultaneously. In this regard, we need to compare our results for our individual fits: Fits A, B, and C. In Fig. 2, some samples of our theoretical predictions for various types of experimental data and their uncertainties at NNLO as a function of x and p_T are displayed.

In Table V, the results of numerical values for the PDF parameters which are described in Sec. III and also $\alpha_s(M_Z^2)$ extracted values are summarized for each fit procedure, and for NLO and NNLO as well.

The extracted values of $\alpha_s(M_Z^2)$ from Fits A and B at the NNLO are 0.1134 ± 0.0024 and 0.1187 ± 0.0007, respectively. These numerical values illustrate how non-LHC experimental data impact $\alpha_s(M_Z^2)$ when we compare it to the world average value of $\alpha_s(M_Z^2) = 0.1179 \pm 0.0085$ [107]. This is a very reasonable result, based on the fact that jet cross-section data impact on $\alpha_s(M_Z^2)$ significantly. This finding was already reported in some previous QCD analysis. For more details, we refer the reader to Ref. [5].

According to Table V, for Fit C, by including LHC data we obtain $\alpha_s(M_Z^2) = 0.1179 \pm 0.0006$ at the NNLO. It seems that LHC data in Table IV change not only the central value of $\alpha_s(M_Z^2)$ but also its uncertainties in comparison to Fit A, in which we use the HERA I + II combined data only.

Figure 3 illustrates the NLO and NNLO QCD fit results for valence, sea, and gluon PDFs as a function of x at $Q^2 = 1.9\ \mathrm{GeV}^2$ for Fit A, Fit B, and Fit C. In the left panels, we present our results for NLO, whereas the right panels are for NNLO. Although there are no significant changes in some PDFs in all fits at NLO (left panels), significant changes in the central value of gluon PDF, their uncertainties, or both are observed from Fit A to Fit C. Such behaviors are also observed at NNLO from Fit A to Fit C (right panels).

To clarify the differences between our QCD fits from Fit A to Fit C, we present the ratios $xq(x, Q^2)/xq(x, Q^2)_{\mathrm{ref}}$ with respect to Fit A at NLO (left panels) and also NNLO (right panels) in Fig. 4. According to this figure, and for both NLO and NNLO analysis, the changes of the central values of all PDFs, their uncertainties, or both are observed at $Q^2 = 1.9\ \mathrm{GeV}^2$.

In Figs. 5 and 6, the results of PDFs based on our three fits, as a function of x for $Q^2 = 3\ \mathrm{GeV}^2$, $Q^2 = 10\ \mathrm{GeV}^2$, and $Q^2 = 100\ \mathrm{GeV}^2$ are presented at NLO and NNLO, respectively. According to these figures, there are not significant changes in the valence or sea PDFs. To investigate the specific impact of the HERA I + II, non-LHC, and LHC data on PDFs in Figs. 5 and 6, we need to compare our results for the relative uncertainties

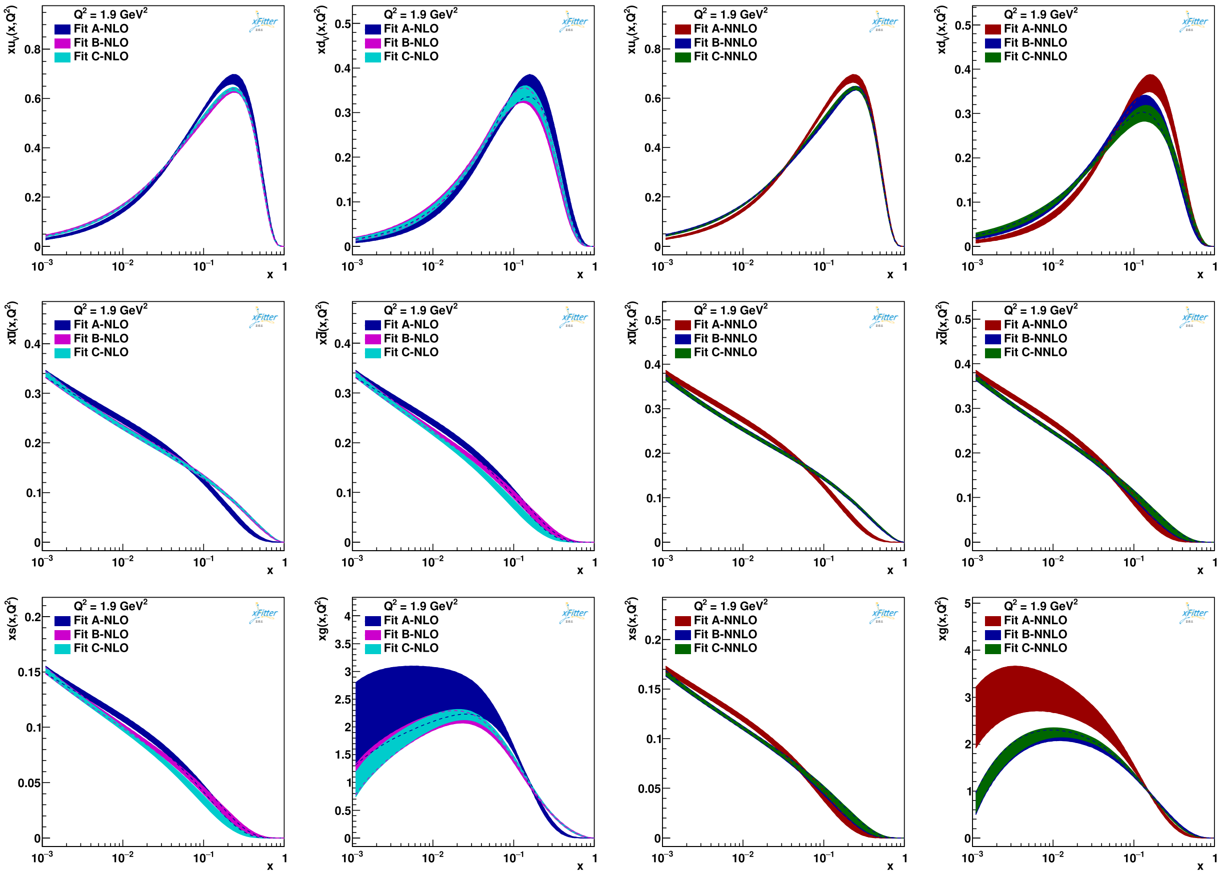

FIG. 3. The NLO and NNLO parton distribution of xu_v, xd_v, $x\bar{u}$, $x\bar{d}$, xs, and xg for Fit A, Fit B, and Fit C extracted as a function of x at $Q^2 = 1.9$ GeV^2. In the left panels, we present our results for NLO, whereas the right panels are for NNLO.

of $\delta xq(x,Q^2)/xq(x,Q^2)$. In Fig. 7, we present the results of the relative uncertainties $\delta xq(x,Q^2)/xq(x,Q^2)$ for $q = u_v, d_v, \Sigma$, and g for the selected scales $Q^2 = 1.9$, 10 GeV^2 as a function of x and for our individual Fits A, B, and C. In the left panels, we present our results for NLO, whereas the right panels are for NNLO. According to this figure, changes of the PDF uncertainties are observed, especially for $\delta x\Sigma(x,Q^2)/x\Sigma(x,Q^2)$ at large x and $\delta xg(x,Q^2)/xg(x,Q^2)$, for both low and large parton x values and for NLO and NNLO. In this figure also, the relative uncertainty ratios for valence PDFs are decreased at low values of x from Fit A to Fit C, obviously. This figure illustrates the impact of the non-LHC and LHC data on PDFs in different ranges of x values when these datasets are added to HERA data.

To investigate the specific impact of LHC data on gluon PDF at large x, we also need to present our results for the relative uncertainties $\delta xg(x,Q^2)/xg(x,Q^2)$ in linear plots. Figure 8 illustrates the NLO and NNLO QCD fit results for the gluon PDF as a function of x at different scale values $Q^2 = 1.9, 3, 5, 10$ GeV^2. In the upper panels, we present our results for NLO, whereas the lower panels are for NNLO. In this figure, significant changes are obtained in the gluon PDF uncertainties at the large-x region in the presence of HERA I + II (Fit A), non-LHC data (Fit B), and LHC data (Fit C). Figure 8 illustrates clearly two significant outcomes: First, one can find how adding non-LHC and LHC datasets to HERA I + II reduce the gluon relative uncertainties at high values of x significantly, as is obvious from results of Fit C where the LHC experimental data are included in the fit procedure. Second, a comparison between these diagrams shows that shifting from NLO to NNLO creates remarkable constraints on gluon PDFs of Fit C, particularly at high x.

For more clarification, a direct comparison between NLO and NNLO results at large x, the relative uncertainties $\delta xg(x,Q^2)/xg(x,Q^2)$ for Fit C as a completed fit procedure are presented in Fig. 9 for different $Q^2 = 10$, 100, 6464, and 8317 GeV^2 values.

Several well-known modern PDFs are also available, which have used almost the same dataset in their analysis. All these groups were looking for a common goal, which is to extract the PDFs using the experimental data.

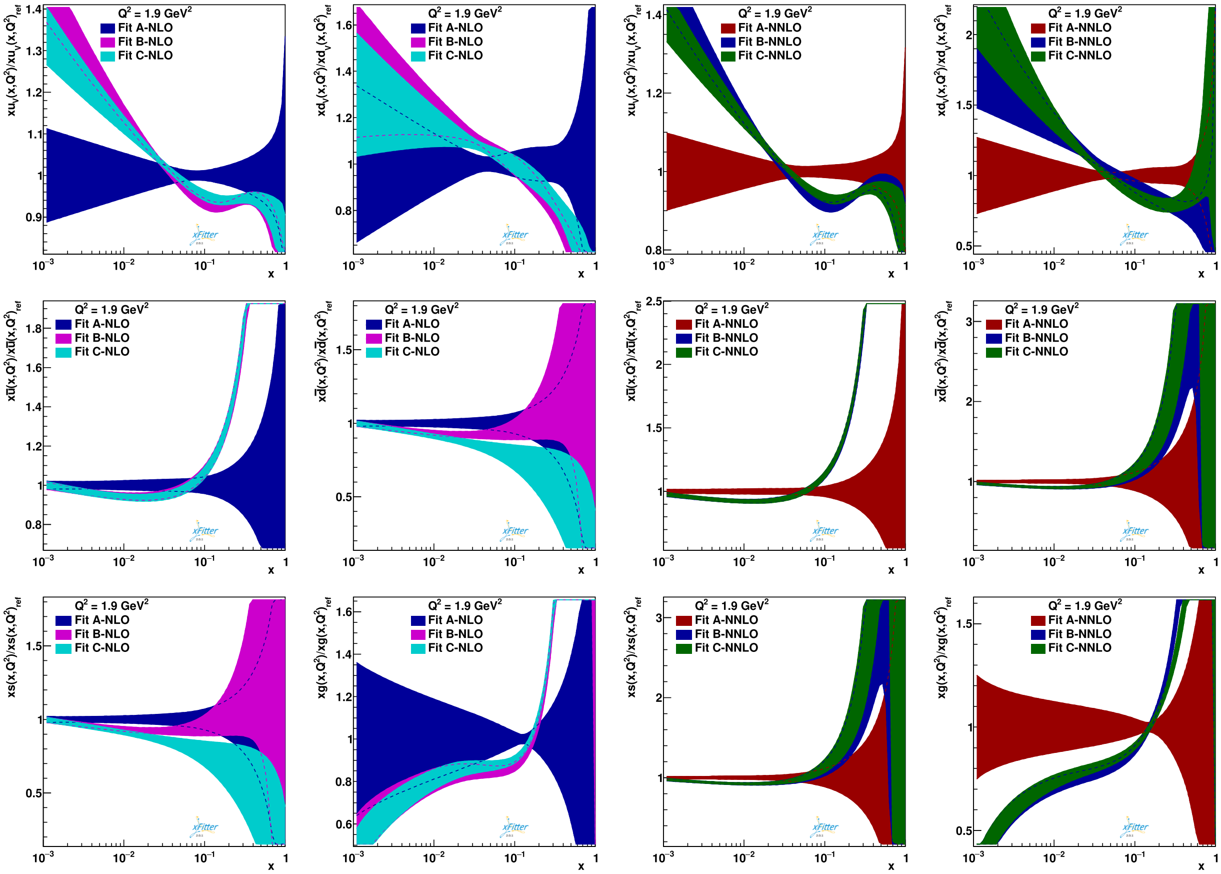

FIG. 4. The NLO and NNLO ratios of $xq(x,Q^2)/xq(x,Q^2)_{\mathrm{ref}}$ at $Q^2 = 1.9$ GeV^2 for $q = u_v, d_v, \bar{u}, \bar{d}, s$, and g for Fit A, Fit B, and Fit C, with respect to Fit A. In the left panels, we present our results for NLO, whereas the right panels are for NNLO.

To investigate the compatibility of main extracted PDFs (i.e., Fit C) at the NNLO with other modern PDF sets such as NNPDF [9] and CT18 [6], for example, we compare our results with the PDF sets that already exist at NNLO. Figure 10 displays the compatibility of our results for Fit C with NNPDF and CT18 for xu_v, xd_v, $x\Sigma$, and xg PDFs as a function of x at 1.9 GeV^2. In this figure, the relative PDF uncertainties $\delta xq(x,Q^2)/xq(x,Q^2)$ are shown in both logarithmic and linear plots. The difference of our analysis from other groups is that we have 14 free parameters and 1891 data points in Fit C, but CT18 and NNPDF are extracted by utilizing 3681 and 4618 data points, respectively, with a very different number of parameters. It seems that, in general, overall good agreement exists between our results and other reported results from modern PDFs at NNLO.

Because the charm PDF benefits from the accuracy of the gluon PDF, it would be very worthwhile to present our results for charm PDF. Undoubtedly, a significant reduction in gluon PDF uncertainty, especially in large x, will reduce the charm PDF uncertainty. In Fig. 11, we present the impact of the LHC data (Fit C) on charm PDF at NNLO in comparison with HERA I + II (Fit A) and non-LHC data (Fit B). The charm PDF with both logarithmic and linear plots, and also the relative uncertainties $\delta xc(x,Q^2)/xc(x,Q^2)$ as functions of x at 3, 5, 10, and 100 GeV^2 are shown with significant reduction on charm PDF uncertainty at large x. This result—i.e., such a reduction of charm PDF uncertainty at large x—can be very worthwhile for future experiments at LHC, and also in some processes in which we need to include the intrinsic charm (IC) with the extrinsic charm PDF. It should be noted that the IC is dominant in the large-x region only.

A. The strong coupling $\alpha_s(M_Z^2)$

In some PDF studies, the value of $\alpha_s(M_Z^2)$ may be considered as a fixed parameter with the world average value [107]. In our fit procedure, we allow the value of $\alpha_s(M_Z^2)$ to vary as a free parameter. In fact, in the present analysis, the strong coupling constant value $\alpha_s(M_Z^2)$ is obtained simultaneously with PDFs at both NLO and NNLO approximations in QCD.

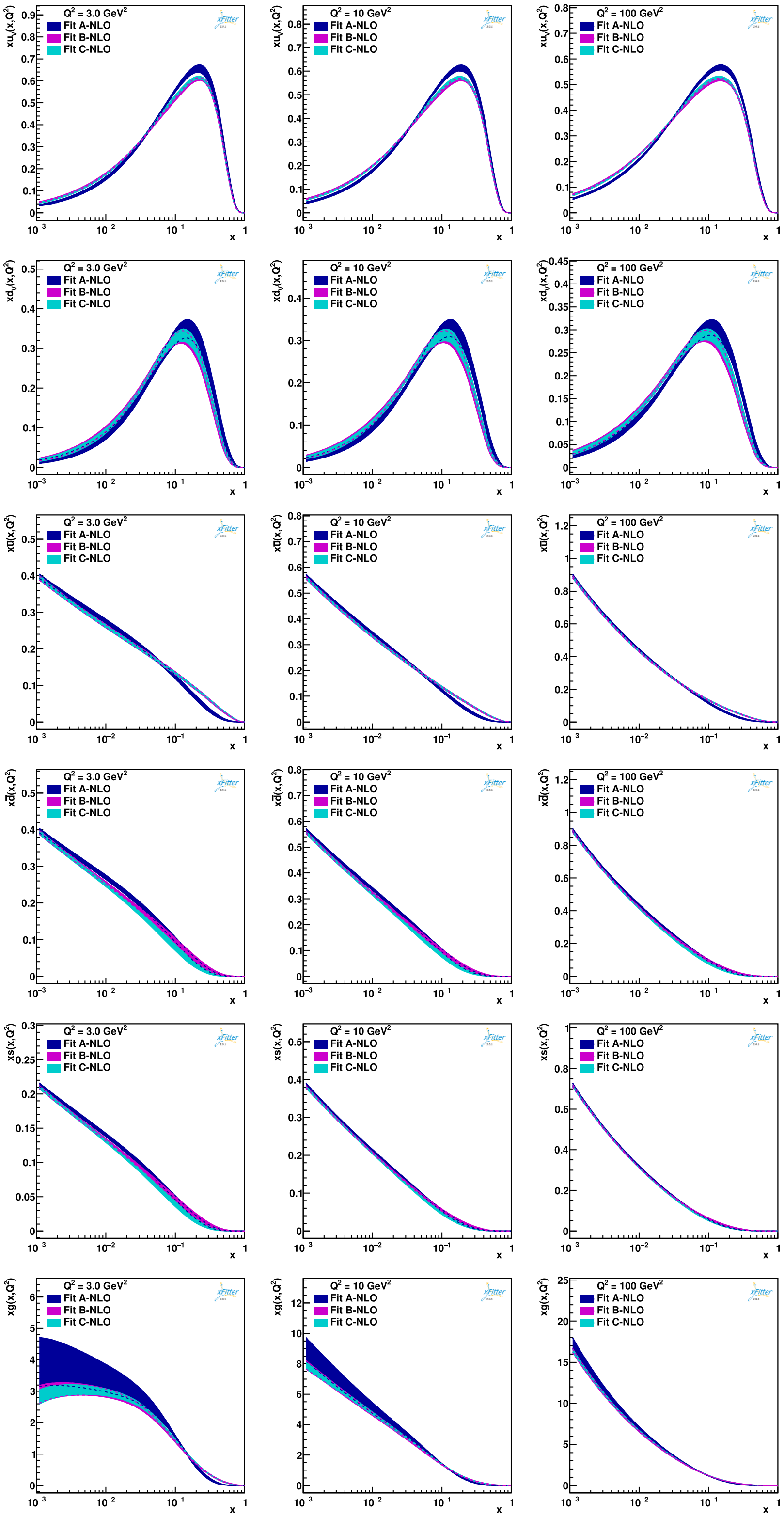

FIG. 5. The NLO parton distribution of xu_v, xd_v, $x\bar{u}$, $x\bar{d}$, xs, and xg, as a function of x and for different values of $Q^2 = 3$, 10, and 100 GeV^2.

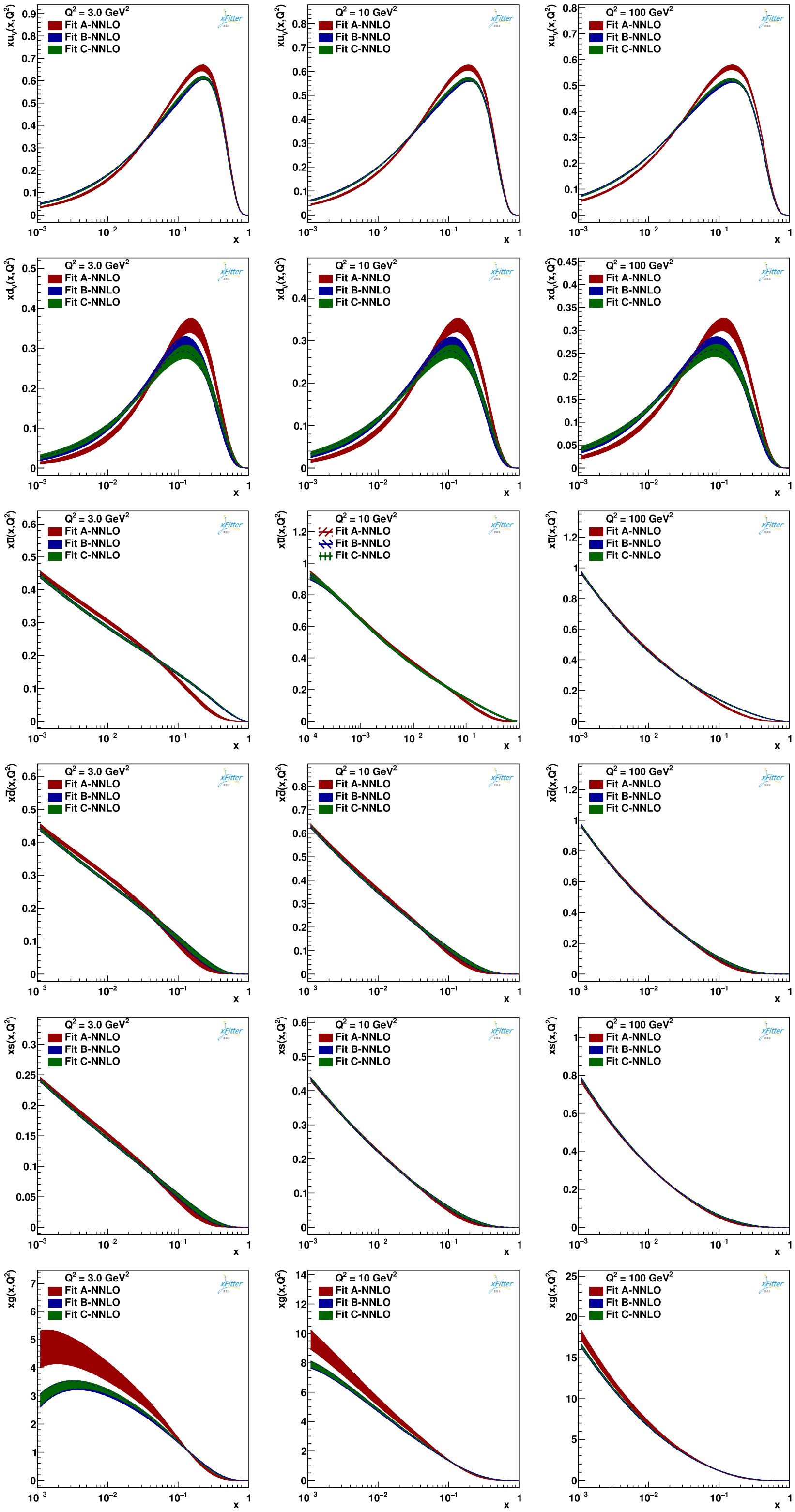

FIG. 6. The NNLO parton distribution of xu_v, xd_v, $x\bar{u}$, $x\bar{d}$, xs, and xg, as a function of x and for different values of $Q^2 = 3$, 10, and 100 GeV^2.

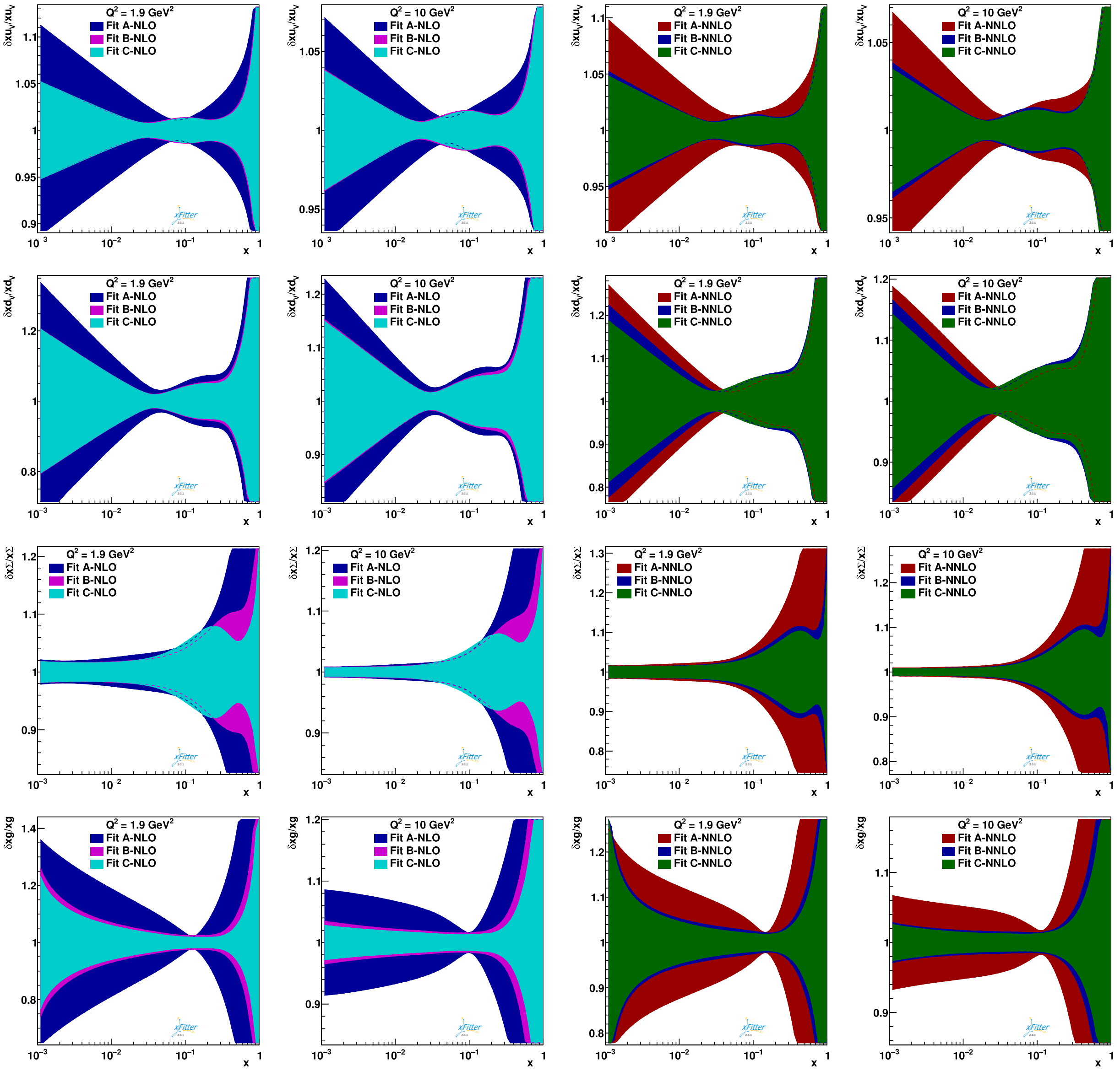

FIG. 7. The NLO and NNLO results of the relative uncertainties $\delta xq(x,Q^2)/xq(x,Q^2)$ for $q = u_v, d_v, \Sigma$, and g at the selected scales $Q^2 = 1.9$, 10 GeV^2 as a function of x and for individual Fits A, B, and C. In the left panels, we present our results for NLO, whereas the right panels are for NNLO.

The different datasets may affect the PDF and strong coupling constant and also their uncertainty extraction. In the present analysis, the strong coupling constant values and their uncertainties are obtained by considering different datasets. The central value of the strong coupling constant, and also its uncertainty, is very sensitive to the gluon PDF and its uncertainty. Since the large-x gluon PDF benefits from an accurate determination of quark PDFs, we find that only the top-quark production and jet cross-section measurements have an impact on the central value and also impact significantly on the uncertainty of gluon PDF and the strong coupling constant.

The different datasets which are listed in Table IV—i.e., HERA I + II data, and the non-LHC and LHC datasets—play an important role in the determination of the strong coupling constant value.

To study the particular significance of these three samples, we consider Fit A without including the non-LHC and LHC datasets. In this case, the values of $\alpha_s(M_Z^2) = 0.1167 \pm 0.0014$ and $\alpha_s(M_Z^2) = 0.1134 \pm 0.0024$ at NLO and NNLO in QCD are obtained. However, they are smaller than the world average value of $\alpha_s(M_Z^2) = 0.1179 \pm 0.0085$ [107].

When the non-LHC data listed in Table IV are added to HERA I + II data in Fit B, we find the values

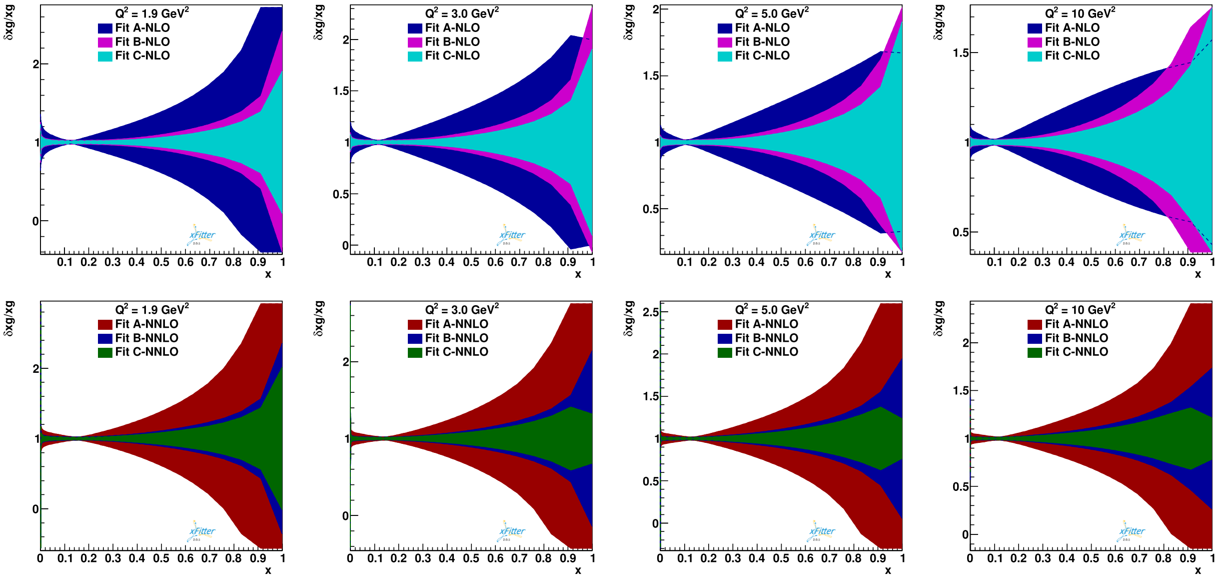

FIG. 8. The impact of the LHC data Fit (C) on the high-x relative uncertainties $\delta xg(x,Q^2)/xg(x,Q^2)$ at NLO and NNLO with comparisons of HERA I + II (Fit A), non-LHC data (Fit B), and LHC data (Fit C). The linear plots of the gluon PDF relative ratio as a function of x are presented at 1.9, 3, 5, and 10 GeV^2. In the upper panels, we present our results for NLO, whereas the lower panels are for NNLO.

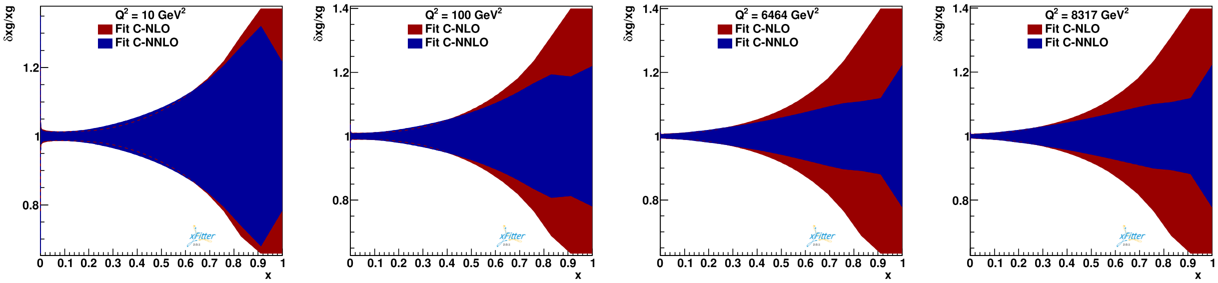

FIG. 9. The comparison of NLO and NNLO gluon relative uncertainties $\delta xg(x,Q^2)/xg(x,Q^2)$ for Fit C as a function of x at $Q^2 = 10$, 100, 6464, and 8317 GeV^2.

$\alpha_s(M_Z^2) = 0.1198 \pm 0.0008$ for NLO and $\alpha_s(M_Z^2) = 0.1187 \pm 0.0007$ for NNLO, which are larger than the $\alpha_s(M_Z^2)$ values that are obtained from the HERA I + II DIS data only, but they have a significantly small statistical error.

Finally, when the LHC data listed in Table IV are included in Fit C, the values of $\alpha_s(M_Z^2) = 0.1188 \pm 0.0007$ and $\alpha_s(M_Z^2) = 0.1179 \pm 0.0006$ are obtained at NLO and NNLO, respectively. These are not very different from the extracted values from Fit B; they have a slightly smaller statistical error, but a significantly smaller statistical error in comparison to Fit A. The main origin of small uncertainty for the strong coupling constant in Fits B and C is related to the significant reduction in the gluon PDF uncertainty, especially at large x in the presence of the top-quark production and jet cross-section measurements. In fact, such a reduction in the gluon PDF uncertainty causes us to extract the small uncertainties for the strong coupling constant.

Other theoretical groups have also determined the value of $\alpha_s(M_Z^2)$ in the PDF fits. The NNLO values $\alpha_s(M_Z^2) = 0.1164 \pm 0.0024$ and $\alpha_s(M_Z^2) = 0.1156 \pm 0.0011$, obtained by the CTEQ [6] and HERAPDF [108] groups, respectively, despite looking similar, have different origins and datasets. Our new results are compatible with the reported results $\alpha_s(M_Z^2) = 0.1147 \pm 0.0008$ at NNLO [109] and $\alpha_s(M_Z^2) = 0.1191 \pm 0.0008$ at NLO [18].

However, in the present analysis, the different datasets listed in Table IV are more or less sensitive to the variation of $\alpha_s(M_Z^2)$. In order to examine the sensitivity

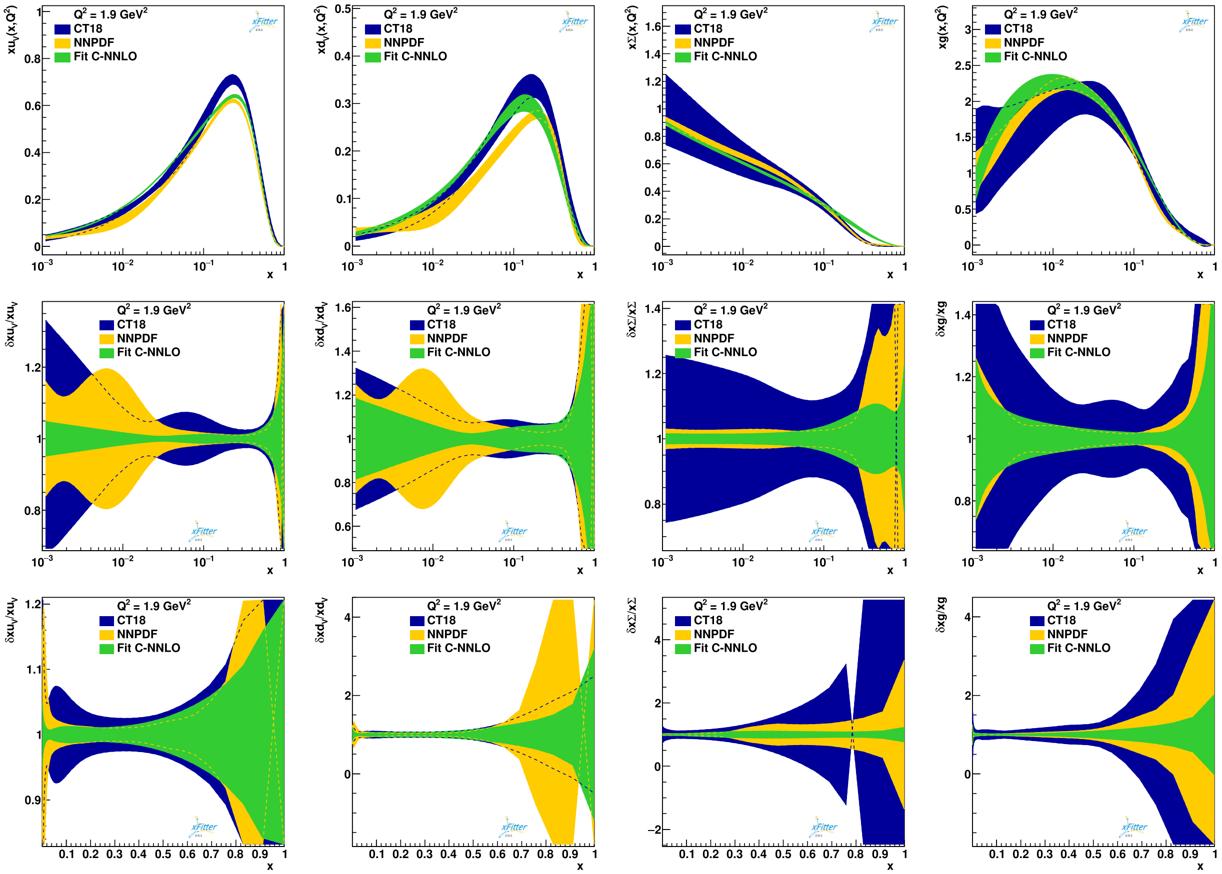

FIG. 10. The compatibility of the main extracted PDF (Fit (C) at NNLO with NNPDF [9] and CT18 [6] for xu_v, xd_v, $x\Sigma$, and xg distribution as a function of x at 1.9 GeV^2. The relative uncertainties $\delta xq(x,Q^2)/xq(x,Q^2)$ PDFs with both logarithmic and linear plots are also presented.

of each dataset to the variation of QCD coupling, we define $\Delta\chi_i^2(a) = \chi_i^2(a) - \chi_i^2(a_{\min})$, as a function of parameter a. Therefore, according to this definition, $\Delta\chi^2_{\text{tot}}(a_{\min}) = 0$. Considering $a = \alpha_s(M_Z^2)$, the values of $\Delta\chi_i^2(\alpha_s(M_Z^2))$ give the difference between the values of χ^2 for experiment i at the fixed value of $\alpha_s(M_Z^2)$ considering the rest of the free parameters, and the value of χ^2 related to same experiment i extracted from one of Fit A, B, or C.

In order to show the sensitivity of the individual datasets, we present in Fig. 12 a series of curves for $\Delta\chi_i^2$ as a function of the strong coupling $\alpha_s(M_Z^2)$ obtained from Fits A, B, and C at NNLO in the scan fit using $\alpha_s(M_Z^2)$ values spanning the range 0.111–0.116 for Fit A, the range 0.116–0.121 for Fit B, and the range 0.116–0.120 for Fit C in units of 0.001 for each type of dataset. The $\Delta\chi^2_{\text{tot}}$ curves for all experiments are also shown, and Fits A, B, and C prefer $\alpha_s(M_Z^2)$ to 0.1134 ± 0.0024, 0.1187 ± 0.0007, and 0.1179 ± 0.0006 at NNLO, respectively.

To summarize, we find that Fit C datasets produce the strongest impact on the QCD coupling value and prefer a slightly smaller value of $\alpha_s(M_Z^2)$ and its uncertainty than in Fit B, and also prefer a larger value of $\alpha_s(M_Z^2)$ and a smaller uncertainty than in Fit A.

In the last part of this section, we are interested in studying the role of the tolerance parameter T for the uncertainty $\alpha_s(M_Z^2)$. According to Hessian formalism, and in order to quantify the physical prediction uncertainties which depend on parton distribution functions, the tolerance parameter T may be considered to correspond to the acceptable fit region [99]. Note that due to a combination of parametrization inflexibility, tensions between datasets, and incomplete theory entering the fit, the error values increase by using a tolerance value. In order to quantify the uncertainties, the variation of χ^2 in the neighborhood of its minimum should be explored. In fact, the minimum will increase χ^2 by an amount $\Delta\chi^2$ by moving the free parameters away from the minimum. In this case, one can introduce the relevant neighborhood of the minimum as $\Delta\chi^2 \leq T^2$ [99], where T is a tolerance parameter. By taking into account $T^2 \approx 16$, the uncertainties of $\alpha_s(M_Z^2)$ for Fits B and C are increased. Note that all uncertainties

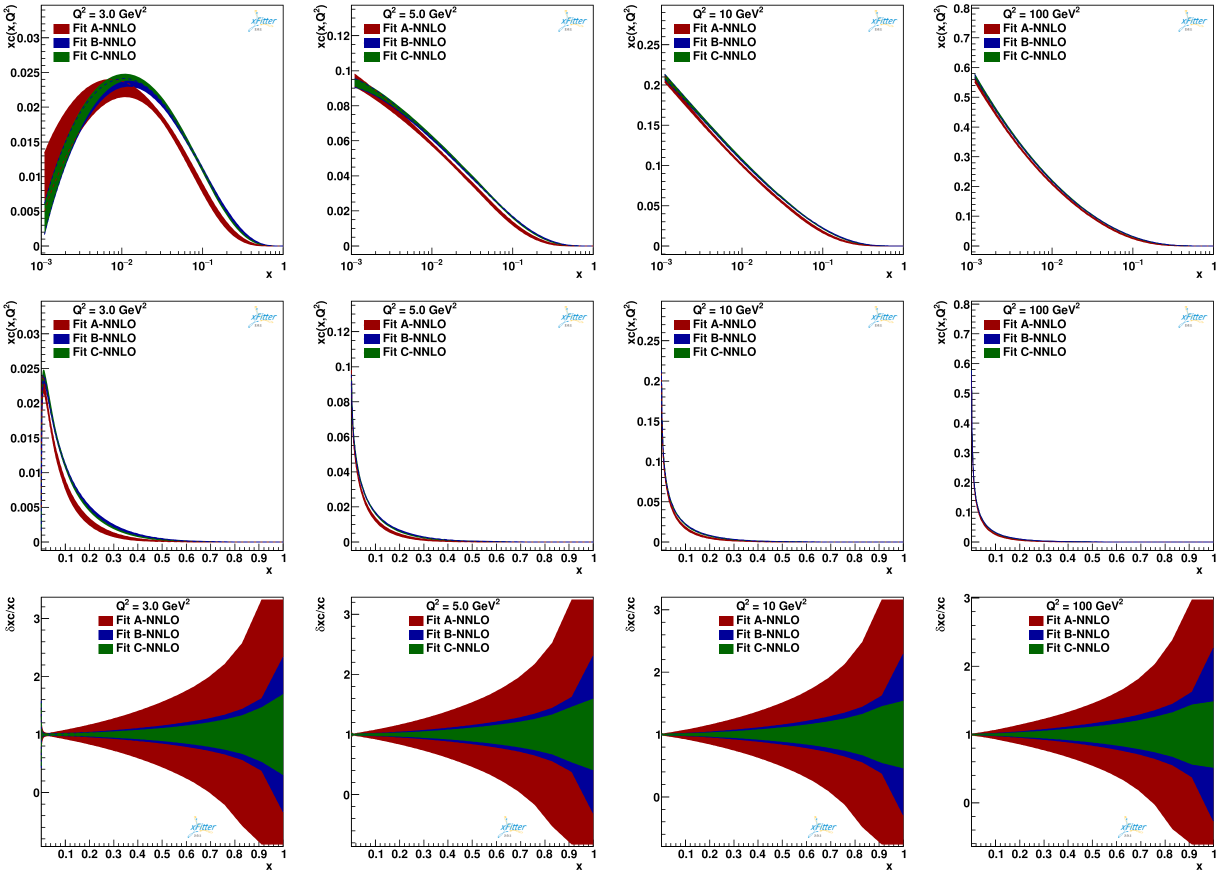

FIG. 11. The impact of the LHC data Fit (C) on the high-x charm PDF at NNLO with comparisons of HERA I + II Fit (A) and non-LHC data (Fit B). The charm PDF with both logarithmic and linear plots and also the relative uncertainties $\delta xc(x, Q^2)/xc(x, Q^2)$ as functions of x at 3, 5, 10 and 100 GeV^2 are presented.

are proportional to T. Using this tolerance value, we obtain the error of $\alpha_s(M_Z^2)$ as 0.0032 and 0.0028 for Fit B, and 0.0028 and 0.0024 for Fit C, at the NLO and NNLO, respectively.

B. Total charm PDFs

As we mentioned before, reducing the uncertainty of gluon distribution with large x produces a strong impact on the charm PDF ("extrinsic charm") in this region. Undoubtedly, such a reduction in the uncertainty of the charm PDF at large x in some processes which are sensitive to the addition of the extrinsic and "intrinsic charm" (IC) contributions would be worthwhile. Note that the IC contribution is dominant only at high x.

In this subsection, we express the full charm PDF by the sum of $xc_{\mathrm{ext}}(x, Q^2)$, which is radiatively generated (perturbative) by the DGLAP equation in our QCD analysis and the $xc_{\mathrm{int}}(x, Q^2)$ (nonperturbative) considering the BHPS model [60,61]. We refer the reader to Ref. [62] as an important review of the intrinsic heavy PDF content of the proton, and to references therein for a detailed discussion of this model. According to the BHPS model, the intrinsic heavy charm distribution is given by

$$c_{\mathrm{int}}(x) = P_{c\bar{c}/p} 1800x^2 \left[\frac{(1-x)}{3}(1 + 10x + x^2) + 2x(1+x)\ln(x)\right]. \tag{7}$$

The above distribution at an initial scale $Q_0 \simeq m_c$ is controlled by nonsinglet evaluation equations [18,77] at any scale. In Fig. 13, we display the intrinsic charm xc_{int} with $P_{c\bar{c}/p} = 1\%$, the extrinsic charm PDF xc_{ext} which is extracted from our QCD Fit C, and also the total charm $xc_{\mathrm{int}} + xc_{\mathrm{ext}}$ distribution as a function of x and for $Q^2 = 5$, 10, 100 GeV^2. In this figure, the uncertainties for $xc_{\mathrm{ext}}(x, Q^2)$ and total charm $xc(x, Q^2)$ are presented as well.

These results facilitate more precise predictions to estimate the impact of a heavy intrinsic contribution on heavy new physics at future facilities such as the Large

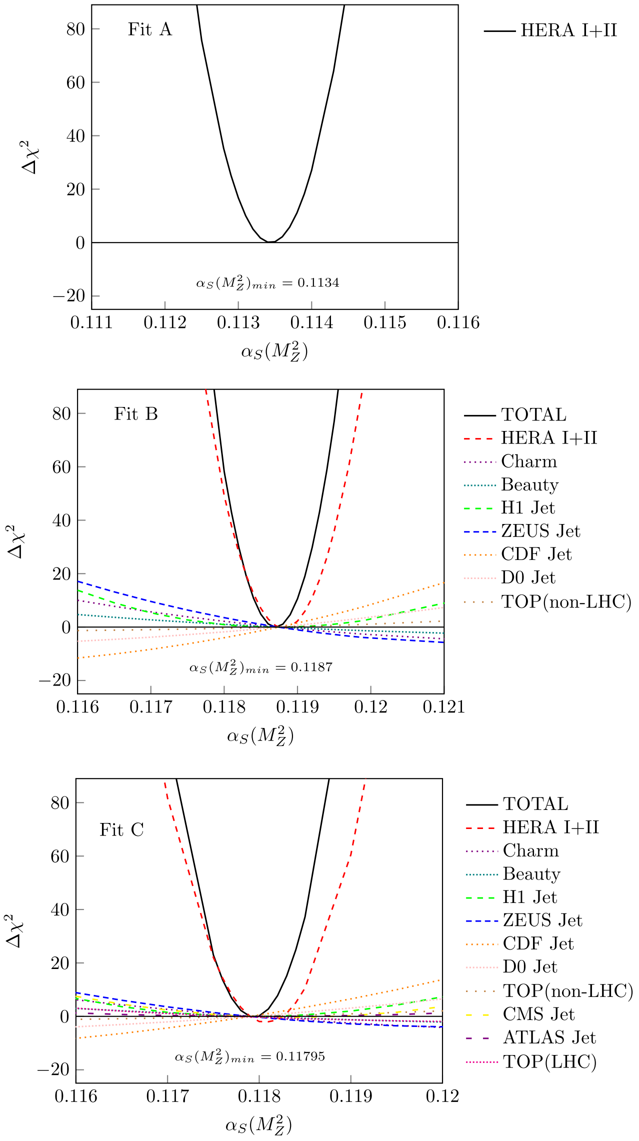

FIG. 12. The scan of the QCD strong coupling constant $\alpha_s(M_Z^2)$ at NNLO precision. Different curves for $\Delta\chi^2$ as a function of strong coupling $\alpha_s(M_Z^2)$ which obtained from the Fit A, B, and C datasets at NNLO and for each type of dataset are presented. The $\Delta\chi^2_{\mathrm{tot}}$ curves for all experiments are also shown.

Hadron-Electron Collider (LHeC), the Electron Ion Collider (EIC), or AFTER@LHC.

C. Higgs boson cross-section prediction using extracted PDFs

In this subsection, we present our predictions for the cross section of the Higgs boson using our extracted PDFs. We determine this cross section at the center-of-mass energies from 6 TeV to 16 TeV using the PDF sets which are extracted from Fit A to Fit C. These calculations have been done using our PDFs and also some modern PDF sets, such as CT18 [6] and NNPDF [9], by utilizing the SusHi-1.7 [110,111] computational package. The theoretical results with a comparison of the experimental measurements for cross sections of H production in pp collisions at the LHC from the ATLAS Collaboration at center-of-mass energies of 8 and 13 TeV [112,113] are shown in Fig. 14. In this figure, we present the theoretical results by considering PDF sets of

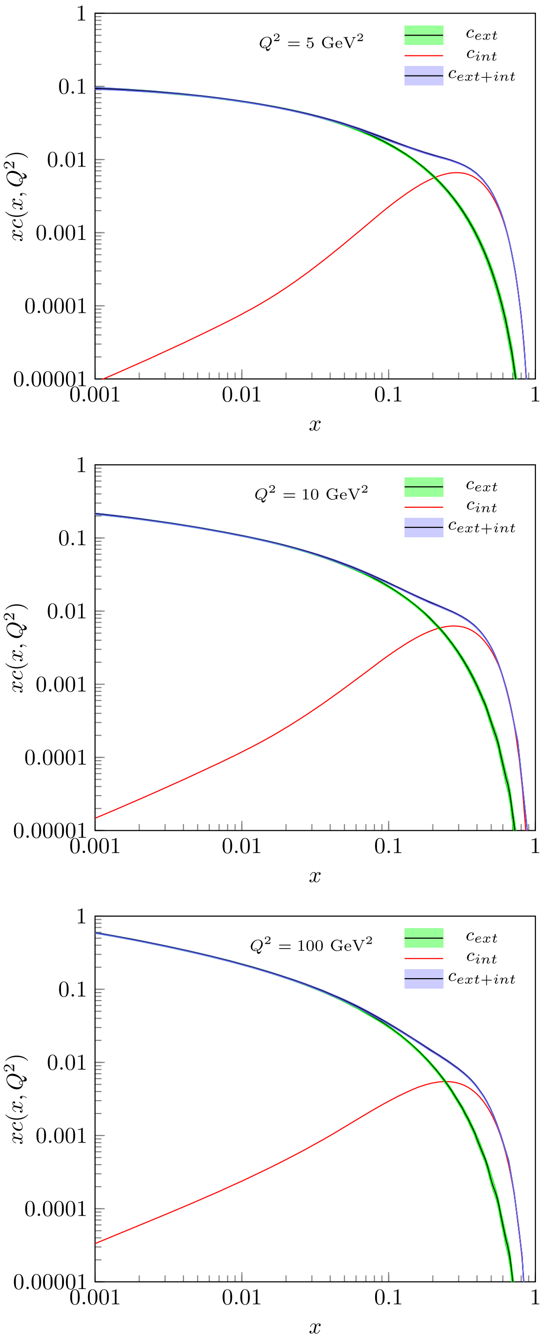

FIG. 13. The intrinsic charm $xc_{\mathrm{int}}(x, Q^2)$, extrinsic charm $xc_{\mathrm{ext}}(x, Q^2)$, and total charm PDF $xc(x, Q^2) = (xc_{\mathrm{int}} + xc_{\mathrm{ext}})(x, Q^2)$, extracted from Fit C as a function of x for $Q^2 = 5$, 10, and 100 GeV^2 with $P_{c\bar{c}/p} = 1\%$. The uncertainties for $xc_{\mathrm{ext}}(x, Q^2)$ and total charm $xc(x, Q^2)$ are presented.

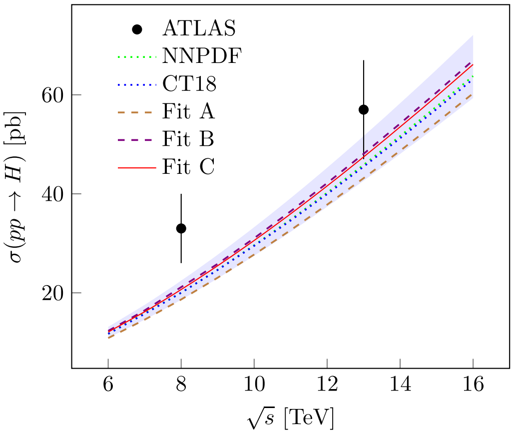

FIG. 14. Comparison between experimental measurements of the cross section of Higgs boson at 8 TeV and 13 TeV center-of-mass energies presented by ATLAS [112,113] and theoretical calculations by considering modern PDF sets NNPDF [9] and CT18 [6], and also our PDF set from Fits A, B, and C at NNLO.

NNPDF [9] and CT18 [6], and our PDF sets which are extracted from Fits A, B, and C; also, the uncertainty related to predictions of Fit C is illustrated in Fig. 14.

The cross-section predictions in this figure display a good agreement between the theory predictions at the NNLO in QCD based on our PDFs and other theoretical models. Our results for Fit C are very close to those of Fit B, and there is an overall good agreement between our results and other PDF sets.

V. CONCLUSION AND DISCUSSION

In this paper, we have presented the parton distribution functions (PDFs), including the HERA I + II DIS experimental data as a base dataset, and both non-LHC and LHC data at NLO and NNLO.

For more clarification about the impact of various types of base, non-LHC, and LHC datasets on PDFs at both NLO and NNLO, we present several fits. The first dataset (Fit A) only contains HERA I + II data to prepare a fine base for investigating the impact of other datasets on PDFs. In the second dataset (Fit B), the non-LHC data are added to the first dataset. And finally, the third dataset (Fit C) contains all previously mentioned data together with LHC measurements. We extract PDFs together with their uncertainties. Also, the values for the QCD strong coupling constant are determined in all datasets.

In this study, one can find how adding non-LHC and LHC data to HERA I + II impacts on the reduction of the gluon relative uncertainties at high values of x significantly, as is obvious from results of Fit C where the LHC experimental data are included in the fit procedure. Also, a comparison between the extracted results shows that shifting from NLO to NNLO creates remarkable constraints on gluon PDFs of Fit C, particularly at high x.

To investigate the specific impact of the HERA I + II, non-LHC, and LHC data on PDFs, we present the relative uncertainty ratios $xq(x,Q^2)/xq(x,Q^2)_{\rm ref}$ with respect to Fit A at NLO and also NNLO. For both NLO and NNLO analysis, the changes of the central values of all PDFs, their uncertainties, or both are observed. The changes of the PDFs uncertainties are observed, especially for $\delta x\Sigma(x,Q^2)/x\Sigma(x,Q^2)$ at large x and $\delta xg(x,Q^2)/xg(x,Q^2)$ for both low and large x values, and for NLO and NNLO. Although there are no significant changes in valence and sea PDFs in all fits at NLO and NNLO, remarkable changes in the central values of gluon PDFs and their uncertainties at large values of x are observed from Fit A to Fit C.

To investigate the compatibility of main extracted PDFs —i.e., Fit C at the NNLO with other modern PDF sets such as NNPDF and CT18—we compared our results with these modern PDF sets. It seems that, in general, overall good agreements between our results and other reported results from modern PDFs at NNLO exist.

We find that the LHC data cause an even more significant impact, not only on the central value of $\alpha_s(M_Z^2)$ but also on its uncertainties in comparison to Fit A, where we use only the HERA I + II combined data. We find that the Fit C dataset produces the strongest impact on the QCD coupling constant and prefers a slightly smaller value and uncertainty for $\alpha_s(M_Z^2)$ compared to Fit B, and also prefers a larger value and smaller uncertainty for $\alpha_s(M_Z^2)$ compared to Fit A.

Because the charm PDF benefits from the accuracy of the gluon PDF, we present our results for the charm PDF with its uncertainty. A significant reduction in gluon PDF uncertainty, especially at large values of x has an impact on the reduction of the charm PDF uncertainty. The reduction of the charm PDF uncertainty at large x can be very worthwhile for future experiments at LHC and also in some processes in which we need to include IC with the extrinsic charm PDF. It should be noted that the IC is dominant at the large-x region only.

In order to benchmark our PDFs, the Higgs boson cross section at the LHC is calculated using modern PDFs and extracts results from Fits A, B, and C showing that they illustrate good compatibility with each other.

ACKNOWLEDGMENTS

M. A. appreciates Daniel Britzger, Alexander Glazov, and Amir Shabanpour for their guidance about computational programs. A. K. is grateful to Stanley Brodsky for valuable discussions, comments, and suggestions. A. K. also appreciates Oleksandr Zenaiev for useful discussion about the XFITTER framework. M. A. also thanks Roberto Di Nardo for useful discussion on theoretical predictions of the Higgs boson cross section. A. K. also is thankful to the CERN TH-PH division for their hospitality and support in which a portion of this work was completed.

[1] A. Khorramian, E. Leader, D. B. Stamenov, and A. Shabanpour, Phys. Rev. D **103**, 054003 (2021).
[2] S. Kumano and Q. T. Song, J. High Energy Phys. 09 (2021) 141.
[3] Y. Zhou *et al.*, N. Sato, and W. Melnitchouk (Jefferson Lab Angular Momentum (JAM)), Phys. Rev. D **105**, 074022 (2022).
[4] Y. Guo, X. Ji, and K. Shiells, Nucl. Phys. **B969**, 115440 (2021).
[5] H. Abramowicz *et al.* (H1 and ZEUS Collaborations), Eur. Phys. J. C **75**, 580 (2015).
[6] T. J. Hou, J. Gao, T. J. Hobbs, K. Xie, S. Dulat, M. Guzzi, J. Huston, P. Nadolsky, J. Pumplin, C. Schmidt *et al.*, Phys. Rev. D **103**, 014013 (2021).
[7] H. Abramowicz *et al.* (H1 and ZEUS Collaborations), Eur. Phys. J. C **75**, 580 (2015).
[8] S. Bailey, T. Cridge, L. A. Harland-Lang, A. D. Martin, and R. S. Thorne, Eur. Phys. J. C **81**, 341 (2021).
[9] R. D. Ball, S. Carrazza, J. Cruz-Martinez, L. Del Debbio, S. Forte, T. Giani, S. Iranipour, Z. Kassabov, J. I. Latorre, E. R. Nocera *et al.*, Eur. Phys. J. C **82**, 428 (2022).
[10] J. Butterworth, S. Carrazza, A. Cooper-Sarkar, A. De Roeck, J. Feltesse, S. Forte, J. Gao, S. Glazov, J. Huston, Z. Kassabov *et al.*, J. Phys. G **43**, 023001 (2016).
[11] T. Han, Y. Ma, and K. Xie, J. High Energy Phys. 02 (2022) 154.
[12] S. Bhattacharya, K. Cichy, M. Constantinou, A. Metz, A. Scapellato, and F. Steffens, Phys. Rev. D **104**, 114510 (2021).
[13] P. Bandyopadhyay and A. Costantini, Phys. Rev. D **103**, 015025 (2021).
[14] C. W. Bauer, N. Ferland, and B. R. Webber, J. High Energy Phys. 08 (2017) 036.
[15] J. Gao, L. Harland-Lang, and J. Rojo, Phys. Rep. **742**, 1 (2018).
[16] M. Mangano, H. Satz, and U. Wiedermann, Report No. CERN-2004-009.
[17] H. W. Lin *et al.*, Prog. Part. Nucl. Phys. **100**, 107 (2018).
[18] H. Abdolmaleki and A. Khorramian, Phys. Rev. D **99**, 116019 (2019).
[19] S. Taheri Monfared, Z. Haddadi, and A. N. Khorramian, Phys. Rev. D **89**, 074052 (2014).
[20] F. Arbabifar, A. N. Khorramian, and M. Soleymaninia, Phys. Rev. D **89**, 034006 (2014).
[21] M. Azizi, A. Khorramian, H. Abdolmaleki, and S. Paktinat Mehdiabadi, Int. J. Mod. Phys. A **33**, 1850142 (2018).
[22] A. Aleedaneshvar and A. N. Khorramian, Nucl. Phys. **A979**, 215 (2018).
[23] S. Rostami, A. Khorramian, and A. Aleedaneshvar, J. Phys. G **43**, 055001 (2016).
[24] A. Radyushkin and S. Zhao, J. High Energy Phys. 02 (2022) 163.
[25] A. Radyushkin and S. Zhao, J. High Energy Phys. 12 (2021) 010.
[26] J. Karpie, K. Orginos, A. Radyushkin, and S. Zafeiropoulos (HadStruc Collaboration), J. High Energy Phys. 11 (2021) 024.
[27] G. Aad *et al.* (ATLAS Collaboration), J. High Energy Phys. 07 (2021) 223.
[28] L. Del Debbio, T. Giani, J. Karpie, K. Orginos, A. Radyushkin, and S. Zafeiropoulos, J. High Energy Phys. 02 (2021) 138.
[29] I. Helenius, M. Walt, and W. Vogelsang, Phys. Rev. D **105**, 094031 (2022).
[30] S. Shen, P. Ru, and B. W. Zhang, Phys. Rev. D **105**, 096025 (2022).
[31] Y. Liu, S. Xu, C. Mondal, X. Zhao, and J. P. Vary (BLFQ Collaboration), Phys. Rev. D **105**, 094018 (2022).
[32] J. L. Zhang, M. Y. Lai, H. S. Zong, and J. L. Ping, Nucl. Phys. **B966**, 115387 (2021).
[33] M. Salimi-Amiri, A. Khorramian, H. Abdolmaleki, and F. I. Olness, Phys. Rev. D **98**, 056020 (2018).
[34] R. Abdul Khalek, R. Gauld, T. Giani, E. R. Nocera, T. R. Rabemananjara, and J. Rojo, Eur. Phys. J. C **82**, 507 (2022).
[35] S. Chekanov *et al.* (ZEUS Collaboration), Phys. Lett. B **547**, 164 (2002).
[36] S. Chekanov *et al.* (ZEUS Collaboration), Nucl. Phys. **B765**, 1 (2007).
[37] H. Abramowicz *et al.* (ZEUS Collaboration), Eur. Phys. J. C **70**, 965 (2010).
[38] A. Aktas *et al.* (H1 Collaboration), Phys. Lett. B **653**, 134 (2007).
[39] F. D. Aaron *et al.* (H1 Collaboration), Eur. Phys. J. C **65**, 363 (2010).
[40] F. D. Aaron *et al.* (H1 Collaboration), Eur. Phys. J. C **67**, 1 (2010).
[41] V. Andreev *et al.* (H1 Collaboration), Eur. Phys. J. C **75**, 65 (2015).
[42] H. Abramowicz *et al.* (H1 and ZEUS Collaborations), Eur. Phys. J. C **78**, 473 (2018).
[43] V. Khachatryan *et al.* (CMS Collaboration), J. High Energy Phys. 03 (2017) 156.
[44] G. Aad *et al.* (ATLAS Collaboration), Eur. Phys. J. C **73**, 2509 (2013).
[45] G. Aad *et al.* (ATLAS Collaboration), Phys. Rev. D **86**, 014022 (2012).
[46] T. Aaltonen *et al.* (CDF Collaboration), Phys. Rev. D **78**, 052006 (2008); **79**, 119902(E) (2009).
[47] V. M. Abazov *et al.* (D0 Collaboration), Phys. Rev. Lett. **101**, 062001 (2008).
[48] T. A. Aaltonen *et al.* (CDF and D0 Collaborations), Phys. Rev. D **89**, 072001 (2014).
[49] B. Abbott *et al.* (D0 Collaboration), Phys. Rev. D **60**, 012001 (1999).
[50] V. Khachatryan *et al.* (CMS Collaboration), Eur. Phys. J. C **77**, 15 (2017).
[51] V. Khachatryan *et al.* (CMS Collaboration), J. High Energy Phys. 08 (2016) 029.
[52] A. M. Sirunyan *et al.* (CMS Collaboration), Eur. Phys. J. C **79**, 368 (2019).
[53] C. V. Villalba (CMS Collaboration), arXiv:2110.13510.
[54] S. Chatrchyan *et al.* (CMS Collaboration), Eur. Phys. J. C **73**, 2339 (2013).
[55] The ATLAS collaboration, Measurement of the $t\bar{t}$ production cross section using dilepton events in pp collisions at $\sqrt{s} = 5.02$ TeV with the ATLAS detector, Report No. ATLAS-CONF-2021-003.

[56] M. Aaboud *et al.* (ATLAS Collaboration), J. High Energy Phys. 02 (2017) 117.
[57] The ATLAS Collaboration, Report No. ATLAS-CONF-2017-054.
[58] G. Aad *et al.* (ATLAS Collaboration), Phys. Rev. D **90**, 072004 (2014).
[59] M. Czakon, N. P. Hartland, A. Mitov, E. R. Nocera, and J. Rojo, J. High Energy Phys. 04 (2017) 044.
[60] S. J. Brodsky, P. Hoyer, C. Peterson, and N. Sakai, Phys. Lett. **93B**, 451 (1980).
[61] S. J. Brodsky, C. Peterson, and N. Sakai, Phys. Rev. D **23**, 2745 (1981).
[62] S. J. Brodsky, A. Kusina, F. Lyonnet, I. Schienbein, H. Spiesberger, and R. Vogt, Adv. High Energy Phys. **2015**, 231547 (2015).
[63] S. J. Brodsky, Novel phenomena in QCD: Heavy flavor and Higgs production at high x_F from intrinsic heavy quarks, http://cds.cern.ch/record/2759499.
[64] G. Lykasov *et al.* (ATLAS Collaboration), Proc. Sci., LC2019 (**2020**) 060.
[65] S. J. Brodsky, K. Y. J. Chiu, J. P. Lansberg, and N. Yamanaka, Phys. Lett. B **783**, 287 (2018).
[66] S. J. Brodsky, Eur. Phys. J. A **52**, 220 (2016).
[67] S. Dulat, T. J. Hou, J. Gao, J. Huston, J. Pumplin, C. Schmidt, D. Stump, and C.-P. Yuan, Phys. Rev. D **89**, 073004 (2014).
[68] J. Pumplin, Phys. Rev. D **73**, 114015 (2006).
[69] J. Blumlein, Phys. Lett. B **753**, 619 (2016).
[70] S. J. Brodsky, V. A. Bednyakov, G. I. Lykasov, J. Smiesko, and S. Tokar, Prog. Part. Nucl. Phys. **93**, 108 (2017).
[71] S. Koshkarev and V. Anikeev, Phys. Lett. B **765**, 171 (2017).
[72] J. C. Anjos, J. Magnin, and G. Herrera, Phys. Lett. B **523**, 29 (2001).
[73] L. M. Montano and G. Herrera, Phys. Lett. B **381**, 337 (1996).
[74] V. A. Bednyakov, M. A. Demichev, G. I. Lykasov, T. Stavreva, and M. Stockton, Phys. Lett. B **728**, 602 (2014).
[75] W. C. Chang and J. C. Peng, Phys. Rev. D **92**, 054020 (2015).
[76] C. S. An and B. Saghai, Phys. Rev. D **95**, 074015 (2017).
[77] F. Lyonnet, A. Kusina, T. Ježo, K. Kovarík, F. Olness, I. Schienbein, and J. Y. Yu, J. High Energy Phys. 07 (2015) 141.
[78] S. J. Brodsky, A. S. Goldhaber, B. Z. Kopeliovich, and I. Schmidt, Nucl. Phys. **B807**, 334 (2009).
[79] R. S. Sufian, T. Liu, A. Alexandru, S. J. Brodsky, G. F. de Téramond, H. G. Dosch, T. Draper, K. F. Liu, and Y. B. Yang, Phys. Lett. B **808**, 135633 (2020).
[80] M. Botje, Comput. Phys. Commun. **182**, 490 (2011).
[81] A. Vogt, Comput. Phys. Commun. **170**, 65 (2005).
[82] T. Carli, D. Clements, A. Cooper-Sarkar, C. Gwenlan, G. P. Salam, F. Siegert, P. Starovoitov, and M. Sutton, Eur. Phys. J. C **66**, 503 (2010).
[83] T. Kluge, K. Rabbertz, and M. Wobisch, arXiv:hep-ph/0609285.
[84] M. Aliev, H. Lacker, U. Langenfeld, S. Moch, P. Uwer, and M. Wiedermann, Comput. Phys. Commun. **182**, 1034 (2011).
[85] xFitter, An open source QCD fit framework, http://xFitter.org.
[86] S. Alekhin *et al.*, Eur. Phys. J. C **75**, 304 (2015).
[87] A. G. Tooran, A. Khorramian, and H. Abdolmaleki, Phys. Rev. C **99**, 035207 (2019).
[88] A. Vafaee and A. N. Khorramian, Nucl. Phys. **B921**, 472 (2017).
[89] A. D. Martin, W. J. Stirling, R. S. Thorne, and G. Watt, Eur. Phys. J. C **63**, 189 (2009).
[90] M. Czakon, M. L. Mangano, A. Mitov, and J. Rojo, J. High Energy Phys. 07 (2013) 167.
[91] Y. L. Dokshitzer, Zh. Eksp. Teor. Fiz. **73**, 1216 (1977) [Sov. Phys. JETP **46**, 641 (1977)].
[92] V. N. Gribov and L. N. Lipatov, Yad. Fiz. **15**, 781 (1972) [Sov. J. Nucl. Phys. **15**, 438 (1972)].
[93] G. Altarelli and G. Parisi, Nucl. Phys. **B126**, 298 (1977).
[94] R. S. Thorne and R. G. Roberts, Phys. Rev. D **57**, 6871 (1998).
[95] J. Blümlein, P. Marquard, C. Schneider, and K. Schönwald, J. High Energy Phys. 11 (2022) 156.
[96] F. James and M. Roos, Comput. Phys. Commun. **10**, 343 (1975).
[97] F. D. Aaron *et al.* (H1 and ZEUS Collaborations), J. High Energy Phys. 01 (2010) 109.
[98] M. Hirai, S. Kumano, T. H. Nagai, and K. Sudoh, Phys. Rev. D **75**, 094009 (2007).
[99] J. Pumplin, D. Stump, R. Brock, D. Casey, J. Huston, J. Kalk, H. L. Lai, and W. K. Tung, Phys. Rev. D **65**, 014013 (2001).
[100] J. Pumplin, D. R. Stump, J. Huston, H. L. Lai, P. M. Nadolsky, and W. K. Tung, J. High Energy Phys. 07 (2002) 012.
[101] A. D. Martin, R. G. Roberts, W. J. Stirling, and R. S. Thorne, Eur. Phys. J. C **28**, 455 (2003).
[102] J. Blumlein and H. Bottcher, Nucl. Phys. **B636**, 225 (2002).
[103] M. Hirai, S. Kumano, and N. Saito, Phys. Rev. D **74**, 014015 (2006).
[104] E. Leader, A. V. Sidorov, and D. B. Stamenov, Phys. Rev. D **73**, 034023 (2006).
[105] D. de Florian, G. A. Navarro, and R. Sassot, Phys. Rev. D **71**, 094018 (2005).
[106] M. Hirai, S. Kumano, and T. H. Nagai, Phys. Rev. C **70**, 044905 (2004).
[107] P. A. Zyla *et al.* (Particle Data Group), Prog. Theor. Exp. Phys. **2020**, 083C01 (2020).
[108] I. Abt *et al.* (H1 and ZEUS Collaborations), Eur. Phys. J. C **82**, 243 (2022).
[109] S. Alekhin, J. Blümlein, S. Moch, and R. Placakyte, Phys. Rev. D **96**, 014011 (2017).
[110] R. V. Harlander, S. Liebler, and H. Mantler, Comput. Phys. Commun. **184**, 1605 (2013).
[111] R. V. Harlander, S. Liebler, and H. Mantler, Comput. Phys. Commun. **212**, 239 (2017).
[112] G. Aad *et al.* (ATLAS Collaboration), Phys. Rev. Lett. **115**, 091801 (2015).
[113] M. Aaboud *et al.* (ATLAS Collaboration), Phys. Lett. B **786**, 114 (2018).